



# Provenance Variability of the Triassic Strata in the Turpan-Hami Basin: Detrital Zircon Record of Indosinian Tectonic Reactivation in the Eastern Tianshan

ZHANG Shaohua<sup>1,2</sup>, LIU Chiyang<sup>3,\*</sup>, BAI Jianke<sup>3,4</sup>, WANG Jianqiang<sup>3</sup>, MA Ming<sup>3</sup>, GUAN Yuzhao<sup>3</sup> and PENG Heng<sup>3</sup>

<sup>1</sup> Shaanxi Key Laboratory of Petroleum Accumulation Geology, Xi'an Shiyou University, Xi'an 710065, China

<sup>2</sup> School of Earth Sciences and Engineering, Xi'an Shiyou University, Xi'an 710065, China

<sup>3</sup> State Key Laboratory of Continental Dynamics, Department of Geology, Northwest University, Xi'an 710069, China

<sup>4</sup> Research Center of Orogenic Geology, Xi'an Center of Geological Survey, China Geological Survey, Xi'an 710054, China

**Abstract:** The Triassic strata in the Turpan-Hami Basin potentially chronicled the missing sedimentary record of Indosinian tectonic evolution in the Eastern Tianshan. In this study, we conducted detrital zircon U-Pb geochronological analyses on subsurface Triassic samples collected from the Turpan-Hami Basin to unravel sedimentary response of Indosinian tectonic reactivation and its geodynamics. The detrital zircon age spectra of the Triassic samples are quite different, reflecting significant provenance variability. The zircon grains in the Lower Triassic sample were mainly from the Central Tianshan, while the Jueluotag acted as a minor provenance. By contrast, the Late Paleozoic rocks in Jueluotag act as the main provenance for the Middle-Upper Triassic samples, while the Central Tianshan acted as a minor provenance. Furthermore, zircon grains in the Middle Triassic sample were mainly from the Permian rocks in Jueluotag, while Indosinian strike-slip-driven rapid exhumation brought deeper Carboniferous rocks of Jueluotag as an important age population for the Upper Triassic sample. The inter-sample variability of age spectra of the Triassic samples provides sedimentary evidence for Indosinian tectonic reactivation in the Eastern Tianshan and its periphery, which could be attributed to differential exhumation of different sources driven by coeval strike-slip tectonics along deep faults. The Indosinian tectonic behavior in the Eastern Tianshan, which is characterized by partial melting of the pre-thickened crust and strike-slip deformation, acted as a far-field respond to the coeval continental accretion occurring along the southern Eurasian margin. Additionally, our new detrital zircon data, together with previously published data in the Turpan-Hami Basin, demonstrate that there are significant changes in source-to-sink system from the Permian to the Triassic, suggesting that the Permian-Triassic unconformity in the Eastern Tianshan and its periphery was generated by Late Permian-Early Triassic tectonic contraction and inversion rather than an increasingly arid climate.

**Key words:** detrital zircon geochronology, provenance, Indosinian tectonic reactivation, Turpan-Hami Basin, Tianshan

Citation: Zhang et al., 2019. Provenance Variability of the Triassic Strata in the Turpan-Hami Basin: Detrital Zircon Record of Indosinian Tectonic Reactivation in the Eastern Tianshan. *Acta Geologica Sinica (English Edition)*, 93(6): 1850–1868. DOI:

## 1 Introduction

The E-W trending Tianshan mountain, situated in the southern part of the Central Asian Orogenic Belt, is traditionally considered to have resulted from the reactivation of the Paleozoic orogen induced by the Cenozoic Indo-Eurasia convergence (Tapponnier and Molnar, 1979; Windley et al., 1990; Hendrix et al., 1994; Dumitru et al., 2001; Jolivet et al., 2010; Tian et al., 2016). However, many lines of evidence (Hendrix et al., 1992; Shao et al., 2001; Greene et al., 2005; Wang et al., 2009; Chen et al., 2011, 2015; Tang et al., 2014, 2015; Fang et al., 2015; Yang Y T et al., 2015, 2017; Han et al., 2016b; Yang W et al., 2017) show that the Tianshan experienced strong intracontinental deformation during the Mesozoic, especially during the Late Mesozoic

(Yanshanian). In contrast, basin analysis of the Junggar Basin suggests that the southern Junggar Basin and its periphery was under a tectonic quiescence setting during the Indosinian stage, and thus inferred that the adjacent Tianshan experienced coeval erosion and planation (Li and Peng, 2013; Tang et al., 2014; Wang et al., 2016, Wang et al., 2018b; Zhu et al., 2017). Recently, Triassic magmatism (Zhang et al., 2005; Zhang et al., 2017a; Zhao H G et al., 2017), contact thermal metamorphism (Mao et al., 2015), exhumation (Gillespie et al., 2017; Yin et al., 2018), endogenous metallization (Zhu, 2007 and references therein; Wu et al., 2017a and references therein), and strike-slip deformation (Chen et al., 2005; Wang et al., 2010; Lei et al., 2018) have been found in the Eastern Tianshan and its periphery, indicating significant Indosinian tectonic reactivation in the Eastern Tianshan. Nevertheless, the sedimentary record of Indosinian

\* Corresponding author. E-mail: lcy@nwu.edu.cn

tectonic reactivation has not been found and thus hampers efforts to better understand the geodynamics of Indosinian tectonic reactivation in the Eastern Tianshan and its periphery.

In this study, we carried out detrital zircon U-Pb geochronological analyses on subsurface Triassic samples collected from Well SC1 in the Turpan-Hami Basin to unravel the sedimentary respond of Indosinian tectonic reactivation in the Eastern Tianshan and its periphery. Then, we integrated new subsurface data with previously published data to elucidate the geodynamics of Indosinian tectonic reactivation in the Eastern Tianshan and its periphery.

## 2 Geological Setting

The E-W trending Tianshan orogenic collage (Fig. 1), extending for more than 2000 km from the NW China to Kazakhstan, Kyrgyzstan, and Tajikistan, is a major part of the Central Asian Orogenic Belt (Şengör et al., 1993; Windley et al., 2007; Xiao et al., 2013). The Tianshan orogenic collage in China, sandwiched between the Tarim Craton to the south and Junggar terrane to the north, is geographically divided into the Western Tianshan and Eastern Tianshan roughly along the Urumqi-Korla transect. Tectonically, the Eastern Tianshan can be divided into three subunits, the South, Central, and North Tianshan units (STS, CTS, NTS in Fig. 1b), which are bounded by suture zones and deep faults (Han and Zhao, 2018 and references therein). The Turpan-Hami Basin is an elongate, east-west-oriented intermontane basin within the Eastern Tianshan, chronicling a long-term intraplate evolutionary history of the Eastern Tianshan and its periphery since the late Paleozoic.

### 2.1 Geology of the Turpan-Hami Basin

The Turpan-Hami Basin (Fig. 2), also known as the Turpan Basin (Graham et al., 1993; Shao et al., 1999) or the Tuha Basin (Han et al., 2016a; Gao et al., 2018), is an intermontane basin with abundant mineral resources such as oil, gas, coal, and uranium (Shao et al., 2003; Wu et al., 2009; Han et al., 2016a; Gao et al., 2018). Tectonically, the Turpan-Hami Basin has a long-term evolutionary history. In terms of the basement of the Turpan-Hami Basin, there are three different viewpoints, including 1) the Precambrian crystalline rocks (Zhang et al., 1984; Xu et al., 2015); 2) Paleozoic oceanic crust, accretionary wedges, and island arcs (Coleman, 1989; Carroll et al., 1990; Zheng et al., 2007); and 3) the hybrids of above two end-members (Wu and Zhao, 1997). Likewise, there have been many different viewpoints on the basin evolution of the Turpan-Hami Basin. The Early Permian magmatism in the Bogda and its periphery implied that the Turpan-Hami Basin was initiated under an extensional setting and there was a unified greater Turpan-Junggar Basin (Allen et al., 1991; Shu et al., 2011). However, the inception of the Turpan-Hami Basin in terms of timing and geodynamics, are still in dispute. Although most researchers agree that the basin initiated during the Early Permian, some studies argue that the basin was initiated as an intracontinental rift during the Carboniferous (Gu et al., 2000; Kuang et al.,

2013). After its inception, some studies suggest that the Turpan-Hami Basin has been evolved as a foreland basin since Late Permian controlled by the development of the northward-vergent Tianshan fold-thrust belt and was separated from the Junggar Basin by the uplift of the Bogda prior to the Early Jurassic (Hendrix et al., 1992; Greene et al., 2005); while other studies argue that the Turpan-Hami Basin experienced three extension-inversion cycles and a stable thermal subsidence stage (Li et al., 1997; Shao et al., 1999, 2003; Tao, 2010; Tian et al., 2017), including: 1) the Carboniferous to middle Permian extension and the tectonic inversion occurred at the end of the Middle Permian; 2) the late Permian to Triassic stable thermal subsidence; 3) the Jurassic extension and latest Jurassic tectonic inversion; and 4) the Cretaceous to Paleogene extension and the tectonic inversion lasted from Neogene to the present.

Structurally, the Turpan-Hami Basin consists of the Turpan Subbasin, Liaoqun Uplift, and Hami Subbasin. The residual sedimentary strata in the Turpan-Hami Basin are largely preserved in the Turpan Subbasin and Hami Subbasin, whereas the Liaoqun Uplift only contains some Lower and Middle Jurassic sediments (Li et al., 1997; Shao et al., 2003). These well-preserved strata reach up to 9000 m thick, including the Carboniferous, Permian, Triassic, Jurassic, Cretaceous, Paleogene, Neogene, and Quaternary from bottom to top (Li et al., 1997; Wu and Zhao, 1997). During the Carboniferous-Early Permian, the sediments within the Turpan-Hami Basin predominantly comprises volcanoclastic rocks and clastic rocks intercalated with lava, while subsequently the sediments mainly consists of terrestrial clastic sediments (Wu and Zhao, 1997). The Triassic strata, the focus of this study, include the Lower Triassic Jiucayuan and Shaofanggou Formations, Middle Triassic Kelamayi Formation, and Upper Triassic Huangshanjie and Haojiagou Formations in an ascending order. The Lower Triassic Jiucayuan and Shaofanggou Formations, known as Upper Cangfanggou Group, consist mainly of red terrestrial clastic sediments. By contrast, the Middle-Upper Triassic Xiaoquangou Group is mainly composed of coarse-grained clastic rocks, dark mudstones and coal seams (Wu and Zhao, 1997).

### 2.2 Regional geology and potential source terranes

As a walled-basin, the Turpan-Hami Basin is likely to have received sediments from all surrounding terranes in the Eastern Tianshan area (Fig. 2). The primary geological features of major tectonic domains in the Eastern Tianshan area have been reviewed by several researchers (Xiao et al., 2004, 2013; Zhang et al., 2016; Han and Zhao, 2018; Huang et al., 2018) and are briefly summarized as follows.

The North Tianshan subunit refers to the region between Kelamaili Fault to the north and Weiya Fault to the south and contains several tectonic belts around the Turpan-Hami Basin, including the Bogda and the Harlik in the north and the Jueluotag in the south (Xiao et al., 2004, 2013). The Bogda is predominantly composed of the Carboniferous strata, including the Lower Carboniferous marine volcanic ignimbrite, tuffaceous sandstone and volcanic lava, and the Upper Carboniferous shallow marine limestone and clastic sediments, associated with

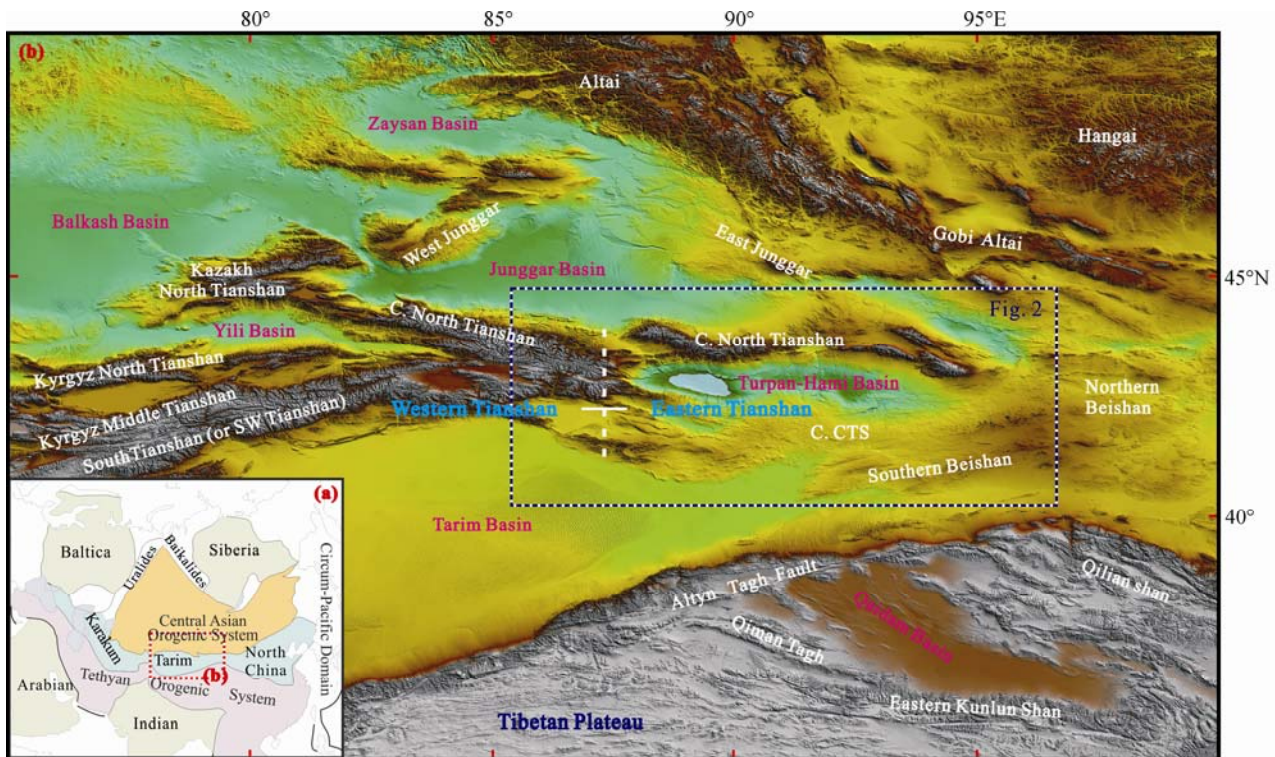


Fig. 1. (a) Simplified tectonic map of eastern Eurasia (modified from Sengör et al., 1993); (b) topographic map of the Tianshan and its adjacent areas.

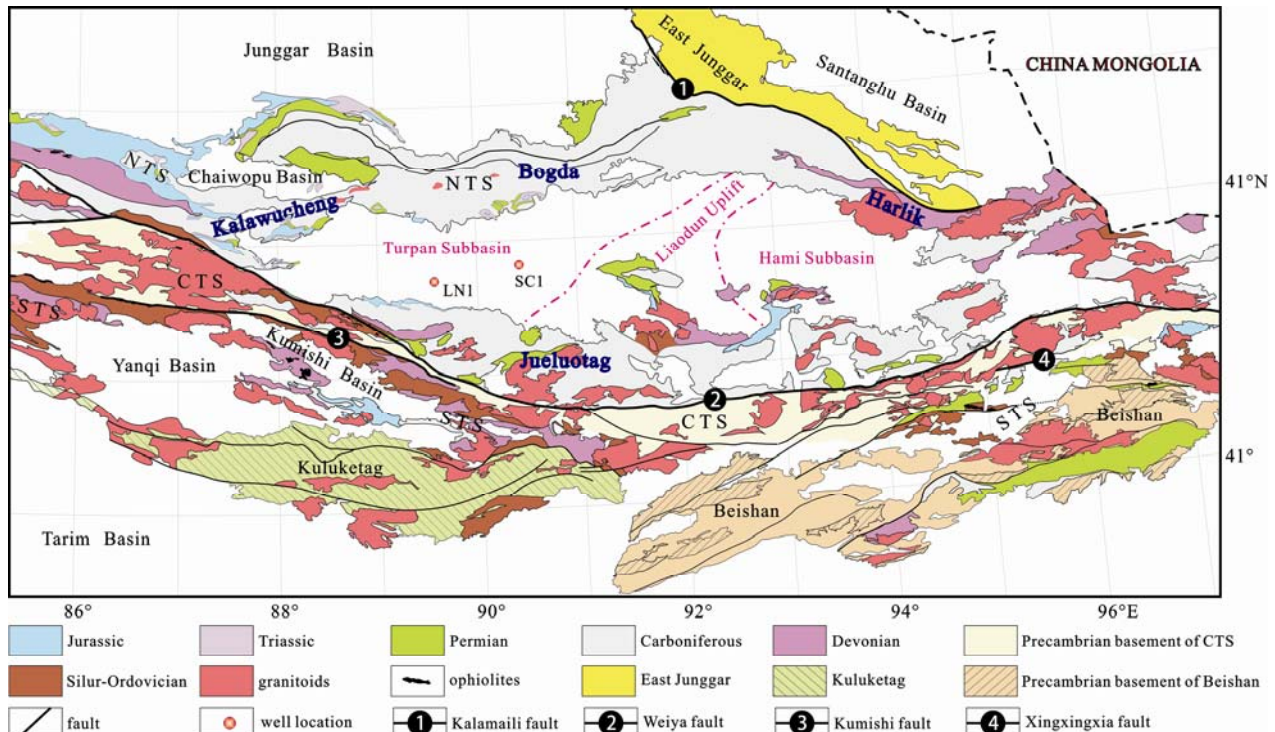


Fig. 2. Simplified geological map and tectonic division of the Eastern Tianshan, modified from Zhang et al. (2016).  
NTS—North Tianshan subunit; CTS—Central Tianshan subunit; STS—South Tianshan subunit.

submarine basalt, andesite, rhyolite, and felsic ignimbrite (Xia et al., 2004, 2008; Xie et al., 2016). The Permian–Mesozoic strata discontinuously distributed along the

piedmont of the Bogda, consisting of the Lower Permian terrestrial clastic sediments intercalated with bimodal volcanic lava, and the Middle Permian–Mesozoic

terrestrial clastic sediments (Xia et al., 2008; Tang et al., 2014; Xie et al., 2016). In brief, intensive Late Paleozoic magmatism occurred in the Bogda and lasted from 350–280 Ma (Wali et al., 2018).

The Jueluotag can be subdivided, from south to north, into the Yamansu belt, the Kangguer shear zone and the Dananhu belt, which are separated by the Yamansu and Kangguer Faults, respectively (Xiao et al., 2004, 2013; Zhang et al., 2017b). The Yamansu belt predominantly comprises the Carboniferous volcanic rocks, including basalts, andesites, and minor rhyolites interbedded with clastic sediments (Xiao et al., 2004; Zhao et al., 2018). The Kangguer shear zone primarily contains the greenschist-facies metamorphosed and ductile-deformed Devonian-Carboniferous volcanic-sedimentary rocks in the southern part, and ophiolitic fragments in the northern part (Shu et al., 1999; Wang et al., 2014). The Dananhu belt mainly consists of the Ordovician to Silurian marine clastics and tuffs with minor limestones and basalts, the Devonian basaltic to felsic volcanic and volcanoclastic rocks, the Carboniferous basalts, basaltic andesites, and rhyolites, with minor sandstones and limestones, and the Permian clastic sediments intercalated with basalts, andesites, and rhyolites (Xiao et al., 2004; Liu et al., 2016). In addition, the Harlik belt has similar stratigraphic succession and rock assemblages with the Dananhu belt (Xiao et al., 2004). To summarize, Paleozoic intrusive and eruptive magmatism occurred pervasively in the Jueluotag belt, with crystallization ages ranging from ~460–260 Ma (Xiao et al., 2004; Han and Zhao, 2018; Huang et al., 2018).

The Central Tianshan subunit, regarded as a Precambrian microcontinent, composed predominantly of Precambrian basement and Paleozoic volcanic-sedimentary rocks (Hu et al., 2000; Huang et al., 2015; Wang et al., 2017). The Precambrian basement rocks have undergone upper-greenschist- to amphibolite-facies metamorphism with major magmatic episodes dated at ~2.5 Ga, ~1.8 Ga, ~1.45–0.65 Ga (Wang et al., 2017 and references therein), while the Paleozoic strata are dominated by Cambrian-Carboniferous greenschists, slates, limestones, and volcanic-siliciclastic rocks. Paleozoic granitic plutons are extensively exposed in the Central Tianshan (Ma et al., 2014), with crystallization ages ranging continuously from ~500–250 Ma (Ma et al., 2014; Huang et al., 2018). In addition, early Mesozoic magmatic reactivation has been revealed in the Central Tianshan and North Tianshan, with crystallization ages ranging from ~250–223 Ma (Zhang et al., 2017a).

The South Tianshan subunit, a wide suture zone resulted from the closure of South Tianshan Ocean between the Central Tianshan and Tarim Craton, is characterized by well-preserved ophiolitic mélange (Gao and Klemd, 2003; Xiao et al., 2004; Gao et al., 2009). The South Tianshan belt is dominated by Silurian to Carboniferous low-to medium-grade and unmetamorphosed successions, and discontinuous ophiolite fragments, high-pressure metamorphic rocks, and granulites (Gao and Klemd, 2003; Xiao et al., 2004, 2013).

### 3 Sampling and Analytical Methods

#### 3.1 Sampling

In this study, three sandstones (samples SC1-2, SC1-3, and SC1-4) were collected from Well SC1 in the southern Turpan-Hami basin. Position and stratigraphic column of the Well SC1 are shown in Fig. 2 and Fig. 3, respectively. Thin section photomicrographs of the samples analyzed in this study are depicted in Fig. 3. Sample SC1-2 from the Upper Triassic Huangshanjie Fm.—Haojiagou Fm. (undivided) is medium-grained lithic sandstone, consisting of abundant volcanic fragments, and a handful of quartzes, feldspars and metamorphic lithics. Sample SC1-3 from the Middle Triassic Kelamayi Fm. is also medium-grained lithic sandstone, which composed of abundant volcanic fragments and a small quantity of quartzes and metamorphic lithics. Sample SC1-4 from the Lower Triassic Jiucayuan Fm.—Shaofanggou Fm. (undivided) is medium-grained lithic sandstone as well, which consists of various lithics, quartzes, feldspars and biotites. Notably, all detrital grains within these samples show poor roundness, reflecting a weak physical modification and short-distance transportation before deposition.

#### 3.2 Zircon separation and Cathodoluminescence (CL) imaging

Zircon grains were separated from the samples, using conventional heavy liquid and magnetic techniques by the Shangyi Geologic Service Co. Ltd, Langfang, Hebei Province, China. Then, 150 zircon grains of every sample were randomly selected and mounted in epoxy resin and polished to expose the grain centres. All the zircon grains were photographed in transmitted and reflected light to characterize their external morphology. Cathodoluminescence (CL) images were obtained using a Quanta 400FEG environmental scanning electron microscope equipped with an Oxford energy dispersive spectroscopy system to evaluate the internal structure of the zircon grains, and then the potential target sites for U-Pb analyses were determined.

#### 3.3 Zircon U-Pb isotope analysis

*In situ* zircon U-Pb and rare earth elements analyses were carried out using an Agilent 7500a quadrupole inductively coupled plasma-mass spectrometer (ICP-MS) and Neptune multiple-collector ICP-MS coupled to a laser at MLR Key Laboratory of Genesis and Exploration of Magmatic Ore Deposits, Xi'an Center of Geological Survey, Xi'an, China. A 193 nm excimer laser was focused on the surfaces of the zircon grains with an energy density of 10 J/cm<sup>2</sup>. A fixed spot size of 30 μm with a laser repetition rate of 5 Hz was adopted throughout this study. Each spot analysis involved the acquisition of 5 s background and 45 s sample data. Helium was used as a carrier gas to transport the ablated aerosol to the laser ablation-ICP-MS (LA-ICP-MS). Each set of six sample analyses was bracketed with analyses of zircon standards 91500 and PLV, and the glass standard NIST SRM 610.  $^{207}\text{Pb}/^{206}\text{Pb}$ ,  $^{206}\text{Pb}/^{238}\text{U}$ ,  $^{207}\text{U}/^{235}\text{U}$ , and  $^{208}\text{Pb}/^{232}\text{Th}$  ratios were corrected for instrumental isotopic and elemental fractionation effects by using the Harvard zircon 91500 as

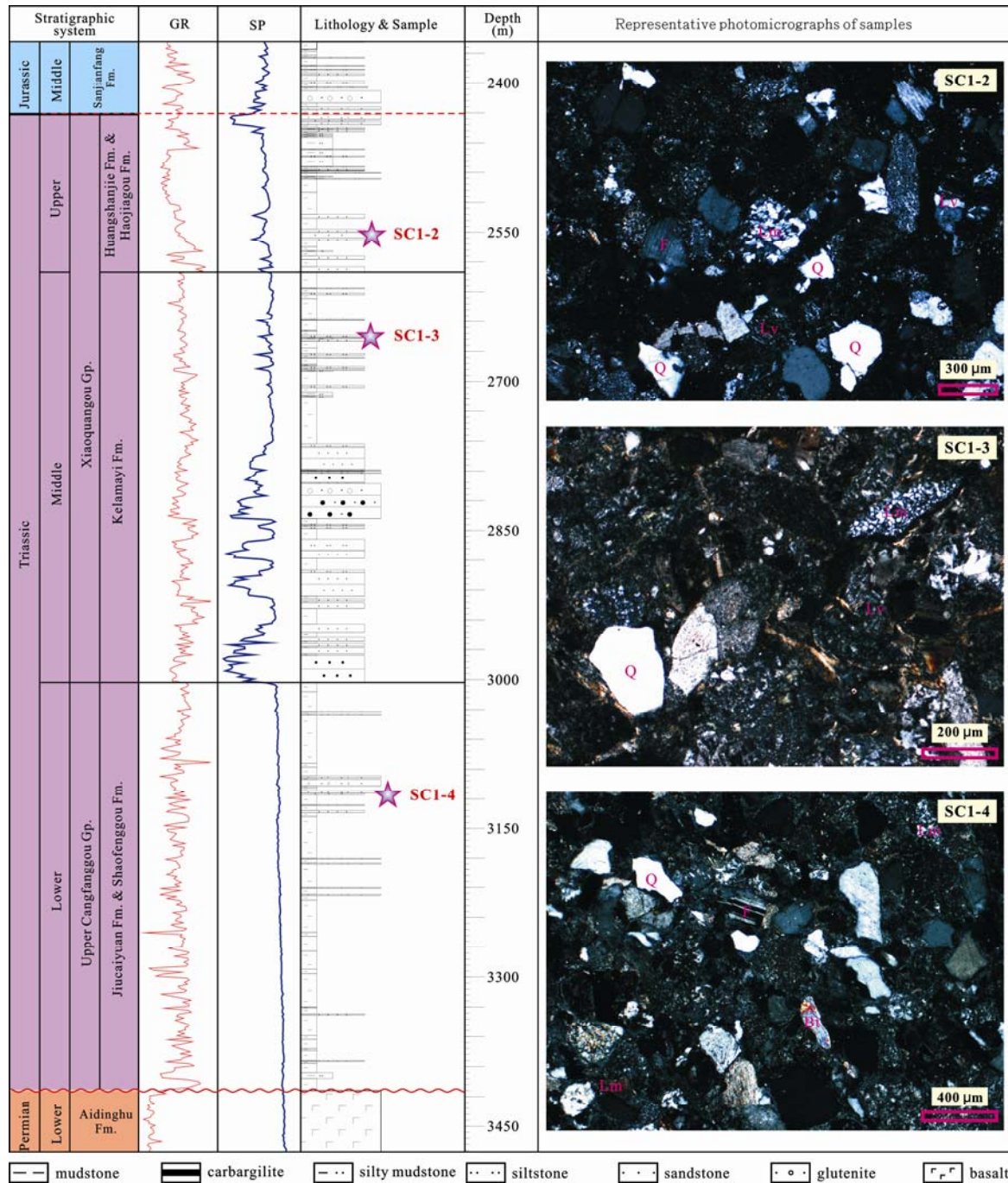


Fig. 3. Stratigraphic column of Well SC1 with positions of samples marked and thin section photomicrographs of the samples analyzed in this study. All photomicrographs are in cross-polarized light.  
Q—quartz; F—feldspar; Bt—biotite; Lm—metamorphic lithic; Lv—volcanic lithic.

an external standard with a recommended  $^{206}\text{Pb}/^{238}\text{U}$  age of  $1065.4 \pm 0.6$  Ma (Wiedenbeck et al., 1995). Trace element concentrations and U-Pb isotopic compositions were calculated using the GLITTER 4.0 program and corrected using  $^{29}\text{Si}$  as an internal standard and NIST SRM 610 as an external standard. Age calculations and plotting of concordia diagrams were performed using Isoplot (v.4.15) (Ludwig, 2012).

About 108–113 grains were carried out for in situ analyses from each zircon target of the samples. The

$^{206}\text{Pb}/^{238}\text{U}$  and  $^{207}\text{Pb}/^{206}\text{Pb}$  ages were used for grains younger than and older than 1000 Ma, respectively. Only concordant or nearly concordant (<10% discordant) isotopic data were considered for interpretation of detrital zircon age.

#### 4 Results

This study analyzed a total of 329 zircon grains for three sandstone samples from Well SC1 in the Turpan-

Hami Basin, and generated 310 concordant ages. Representative cathodoluminescence images of analyzed grains are presented in Fig. 4a. The isotopic information and ages for all the concordant analyses are listed in Table 1, and shown graphically in zircon U-Pb concordia plots (Fig. 5) and histograms with kernel density estimates (KDEs; Fig. 6a).

#### 4.1 Zircon morphology and origin

Analyzed zircon grains are mostly  $>100\text{ }\mu\text{m}$  in the longest dimension and have variable aspect ratios. Although there are a few sub-rounded grains, the majority of zircon grains have poor roundness, implying short-distance transportation. The CL images (Fig. 4a) reveal that most of the zircon grains show fine oscillatory zoning typical of growth in a magmatic environment, while some with inherited cores showing variable CL response that are commonly associated with one or more overgrowths (Corfu, 2003). Zircon Th/U ratios in combination with CL images have commonly been used to determine zircon origin (Belousova et al., 2002). In this study, most of the analyzed zircon crystals have Th/U values greater than 0.1 (Fig. 4b), indicating a typical magmatic origin; while sample SC1-3 and SC1-4 contains a few zircon crystals with Th/U values smaller than 0.1, suggesting a metamorphic origin.

#### 4.2 Zircon U-Pb ages

In the sample SC1-4 from the Lower Triassic, 98 (91%) of 108 grains analyzed were concordant (Fig. 5a). Of the concordant data from sample SC1-4, most (84 grains) have Phanerozoic ages, with the remaining data scattered to Precambrian ages. Kernel density estimates for the data from sample SC1-4 (Fig. 6a) display a broad age population between  $\sim 250$  and  $\sim 500$  Ma, with a major peak at  $\sim 418$  Ma and two lesser peaks at  $\sim 354$  Ma and  $\sim 300$  Ma; the Precambrian age population defines several less well-defined minor peaks at around 914 Ma, 1200 Ma and 1600 Ma.

For the sample SC1-3 from the Middle Triassic, 104 (96%) of 108 grains analyzed plotted on or near the concordia (Fig. 5b), yielding ages between 269 and 2774

Ma. Of the concordant data from sample SC1-3, kernel density estimates (Fig. 6a) show a tight cluster of ages peaking at  $\sim 286$  Ma, a lesser peak at  $\sim 336$  Ma, a minor peak at  $\sim 456$  Ma, and scattered Precambrian ages.

As for the sample SC1-2 from the Upper Triassic, 108 (96%) of 113 grains analyzed yielded reliable concordant ages ranging from 233 to 1878 Ma (Fig. 5c), including 7 grains with Triassic ages. Kernel density estimates for the data from sample SC1-2 (Fig. 6a) define a major peak at  $\sim 320$  Ma, a lesser peak at  $\sim 260$  Ma, and a minor peak at  $\sim 494$  Ma; and the remaining 9 Precambrian ages also display several less well-defined minor peaks.

## 5 Discussions

### 5.1 Sedimentary provenance interpretation

Detrital zircon U-Pb geochronology has been extensively used as a robust method to unravel the provenance of clastic sediments by matching detrital zircon age spectra with the crystallization ages of potential source rocks because zircon has a very high closure temperature during weathering, erosion, deposition and burial in the sedimentary environment (Fedo, 2003; Dickinson and Gehrels, 2009; Thomas, 2011; Cawood et al., 2012; Gehrels, 2014; Zhao et al., 2016; Du et al., 2017; Zhao X C et al., 2017). However, the refractory nature of the U-Pb zircon system implies that it is hard to discern recycled zircon grains and thus lead to an ambiguous interpretation of provenance (Thomas, 2011; Zhang et al., 2019a). In this study, all samples exhibit low compositional and textural maturity (Fig. 3), apparently ruling out multiple recycling and reflecting proximal sedimentation.

Visually, detrital zircon age spectra of the three Triassic samples from Well SC1 in the Turpan-Hami Basin are obviously different (Fig. 6), reflecting varying contributions from different sources. More in detail, the age spectrum of sample SC1-4 shows that the Lower Triassic contains significant peaks of  $\sim 418$  Ma,  $\sim 354$  Ma and  $\sim 300$  Ma and scattered Precambrian ages, indicating significant contribution from Central Tianshan subunit, where is dominated by Paleozoic volcanic-sedimentary

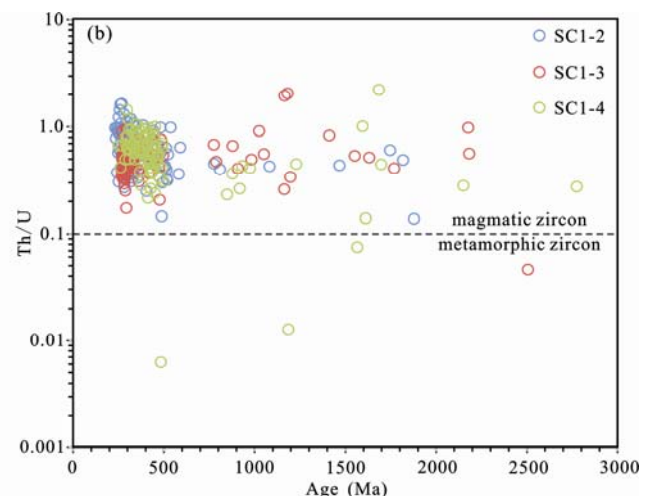
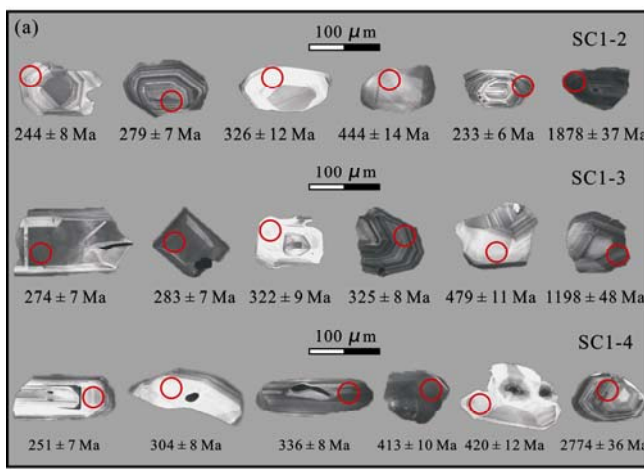


Fig. 4. (a) Representative cathodoluminescence images of selected detrital zircons; (b) diagram of Th/U ratio versus U-Pb age for detrital zircons.

**Table 1** The isotopic information and ages for detrital zircons of the Triassic strata from the Turpan-Hami Basin

Spot	Th conc	U conc	Th/U	$^{207}\text{Pb}/^{206}\text{Pb}$		$^{207}\text{Pb}/^{235}\text{U}$		$^{206}\text{Pb}/^{238}\text{U}$		$^{207}\text{Pb}/^{206}\text{Pb}$		$^{207}\text{Pb}/^{235}\text{U}$		$^{206}\text{Pb}/^{238}\text{U}$		Concor.
				Ratio	1s	Ratio	1s	Ratio	1s	Age±1s (Ma)	Age±1s (Ma)	Age±1s (Ma)	Age±1s (Ma)	Age±1s (Ma)	(%)	
SC1-2	ppm	ppm														
Z2001	29.66	79.55	0.37	0.05132	0.00441	0.27301	0.02295	0.03858	0.00123	255	186.28	245.1	18.3	244	7.62	100.5
Z2002	208.5	225.38	0.93	0.05313	0.00302	0.38184	0.02133	0.05211	0.00145	334.5	123.75	328.4	15.67	327.5	8.91	100.3
Z2003	74.1	190.89	0.39	0.05174	0.0022	0.31549	0.01346	0.04422	0.00111	274	94.58	278.4	10.39	278.9	6.83	99.8
Z2004	358.3	1095.15	0.33	0.05779	0.00133	0.66514	0.01669	0.08347	0.00191	521.6	50.03	517.8	10.18	516.8	11.37	100.2
Z2005	112.04	310.19	0.36	0.05938	0.00156	0.77564	0.02161	0.09473	0.00221	581	56.12	583	12.36	583.5	13.01	99.9
Z2006	200.92	380.93	0.53	0.05214	0.00154	0.33551	0.01033	0.04666	0.0011	291.7	66.09	293.8	7.85	294	6.76	99.9
Z2007	145.01	234.69	0.62	0.05494	0.00177	0.49113	0.01624	0.06483	0.00155	409.9	69.65	405.7	11.06	404.9	9.39	100.2
Z2008	72.77	134.9	0.54	0.05418	0.00226	0.44642	0.01872	0.05976	0.0015	378.3	90.69	374.8	13.14	374.2	9.11	100.2
Z2009	216.58	707.87	0.31	0.05142	0.00175	0.28303	0.00984	0.03993	0.00096	259.5	76.41	253.1	7.79	252.4	5.98	100.3
Z2010	118.19	393.5	0.30	0.05704	0.0015	0.62501	0.01742	0.07948	0.00185	492.4	57.48	493	10.88	493	11.06	100.0
Z2011	136.59	254.96	0.54	0.05318	0.00181	0.38428	0.01341	0.05241	0.00126	336.4	75.46	330.2	9.84	329.3	7.72	100.3
Z2012	127.6	260.61	0.49	0.11117	0.00238	5.19724	0.12361	0.33912	0.00779	1818.6	38.32	1852.2	20.25	1882.5	37.51	96.6
Z2014	138.87	311.15	0.45	0.05259	0.00181	0.35659	0.01252	0.04918	0.00119	311.3	76.38	309.7	9.37	309.5	7.31	100.1
Z2015	13.85	23.54	0.59	0.05293	0.00755	0.37857	0.05318	0.05188	0.00192	325.8	295.02	326	39.17	326.1	11.76	100.0
Z2016	455.42	469.3	0.97	0.05301	0.00207	0.35114	0.01378	0.04805	0.0012	329.2	86.16	305.6	10.36	302.6	7.4	101.0
Z2017	45.58	107.48	0.42	0.05717	0.00255	0.62635	0.02792	0.07948	0.00206	497.5	96.16	493.8	17.43	493	12.31	100.2
Z2018	95.26	238.27	0.40	0.06679	0.00167	1.23145	0.03299	0.13376	0.00312	831.2	51.17	815	15.01	809.3	17.74	100.7
Z2019	194.89	180.59	1.08	0.05179	0.00307	0.30145	0.01754	0.04223	0.00118	276.1	130.21	267.5	13.68	266.6	7.31	100.3
Z2020	99.41	205.45	0.48	0.05301	0.00203	0.37664	0.01457	0.05154	0.00127	329.3	84.49	324.6	10.75	324	7.81	100.2
Z2021	376.17	285.57	1.32	0.05183	0.00195	0.31826	0.01214	0.04455	0.0011	278.1	83.94	280.6	9.35	281	6.78	99.9
Z2022	272.9	273.62	1.00	0.0525	0.00195	0.34828	0.01309	0.04814	0.00119	307.1	82.28	303.4	9.86	303.1	7.29	100.1
Z2023	154.05	179.02	0.86	0.05133	0.0023	0.28483	0.01273	0.04026	0.00103	255.7	99.66	254.5	10.06	254.5	6.38	100.0
Z2024	230.8	188.36	1.23	0.05127	0.00221	0.28183	0.01221	0.03989	0.001	253	96.11	252.1	9.67	252.1	6.19	100.0
Z2025	219.26	369.95	0.59	0.05284	0.00161	0.367	0.01165	0.0504	0.0012	321.8	67.9	317.4	8.65	317	7.36	100.1
Z2026	9.89	21.86	0.45	0.06505	0.00474	1.14912	0.08219	0.12819	0.00406	775.9	146.22	776.8	38.83	777.5	23.18	99.9
Z2027	62.23	110.37	0.56	0.05309	0.0029	0.37696	0.02045	0.05153	0.00137	332.4	119.09	324.8	15.08	323.9	8.4	100.3
Z2028	517.51	500.74	1.03	0.05427	0.00162	0.46038	0.01433	0.06156	0.00147	382.3	65.57	384.5	9.96	385.1	8.91	99.8
Z2029	69.19	125.03	0.55	0.0529	0.00298	0.38055	0.0211	0.05221	0.00146	324.5	122.88	327.4	15.52	328	8.94	99.8
Z2030	63.11	93.95	0.67	0.05313	0.00404	0.38576	0.02885	0.05269	0.00157	334.4	163.29	331.3	21.14	331	9.61	100.1
Z2031	206.19	524.34	0.39	0.05172	0.0015	0.3041	0.00925	0.04267	0.00101	273.1	65.14	269.6	7.2	269.4	6.24	100.1
Z2032	229.22	244.09	0.94	0.05163	0.00214	0.30508	0.01269	0.04288	0.00108	269.2	92.05	270.4	9.88	270.7	6.66	99.9
Z2033	30.91	48.1	0.64	0.05986	0.00328	0.79188	0.0431	0.09601	0.00262	598.6	114.51	592.2	24.42	591	15.41	100.2
Z2034	187.99	193.79	0.97	0.05111	0.00231	0.26994	0.01221	0.03833	0.00097	245.9	100.69	242.6	9.77	242.5	6.04	100.0
Z2035	37.24	83.65	0.45	0.054	0.00279	0.44387	0.02285	0.05966	0.00157	371.1	111.87	373	16.07	373.5	9.56	99.9
Z2037	330.34	573.92	0.58	0.05138	0.00158	0.28031	0.00898	0.0396	0.00094	258	69.1	250.9	7.12	250.3	5.84	100.2
Z2038	45.77	59.91	0.76	0.05578	0.00422	0.54801	0.04039	0.07131	0.00229	443.5	160.09	443.7	26.49	444	13.79	99.9
Z2039	108.54	787.35	0.14	0.11486	0.00239	5.38475	0.12668	0.34032	0.00783	1877.6	37.09	1882.4	20.15	1888.2	37.67	99.4
Z2040	399.38	337.37	1.18	0.0529	0.00179	0.3687	0.01285	0.0506	0.00123	324.4	75.7	318.7	9.53	318.2	7.54	100.2
Z2041	220	397.78	0.55	0.05801	0.0017	0.67789	0.0208	0.08484	0.00203	529.6	63.63	525.5	12.59	524.9	12.05	100.1
Z2042	162.08	171.42	0.95	0.0514	0.00249	0.28211	0.01364	0.03984	0.00102	259	107.32	252.3	10.81	251.9	6.35	100.2
Z2043	90.28	250.59	0.36	0.05254	0.0021	0.35261	0.01424	0.04872	0.00122	308.9	88.59	306.7	10.69	306.7	7.52	100.0
Z2044	29.43	61.83	0.48	0.05587	0.00568	0.55098	0.05472	0.0716	0.00258	446.8	211.73	445.6	35.82	445.8	15.51	100.0
Z2045	104.78	245.57	0.43	0.07554	0.00186	1.85953	0.04957	0.17869	0.00421	1083	48.54	1066.8	17.6	1059.8	23.05	102.2
Z2046	70.04	77.97	0.90	0.05164	0.00587	0.28745	0.03172	0.04041	0.00158	269.6	241.39	256.6	25.01	255.4	9.82	100.5
Z2047	40.02	57.58	0.70	0.05292	0.00504	0.37367	0.03492	0.05127	0.00168	325.1	202.65	322.4	25.81	322.3	10.32	100.0
Z2048	194.13	359.68	0.54	0.05168	0.0019	0.30411	0.01136	0.04273	0.00106	271.1	81.94	269.6	8.85	269.7	6.54	100.0
Z2049	43.27	96.88	0.45	0.05401	0.00351	0.44118	0.02818	0.0594	0.00174	371.3	139.75	371.5	19.85	372	10.6	99.9
Z2050	447.28	413.12	1.08	0.05322	0.00159	0.38993	0.0122	0.0532	0.00127	338.1	66.38	334.3	8.92	334.1	7.8	100.1
Z2051	254.17	252.15	1.01	0.05333	0.00192	0.39774	0.01463	0.05415	0.00134	342.9	79.46	340	10.63	340	8.2	100.0
Z2052	239.31	310.65	0.77	0.05354	0.00167	0.40852	0.01329	0.05541	0.00133	351.6	69.06	347.8	9.58	347.6	8.15	100.1
Z2053	80.87	217	0.37	0.05221	0.00352	0.33188	0.02193	0.04616	0.00137	294.7	146.57	291	16.72	290.9	8.42	100.0
Z2054	151.43	603.32	0.25	0.05492	0.00141	0.49016	0.01359	0.06481	0.00153	408.9	55.88	405	9.26	404.8	9.23	100.0
Z2055	163.45	283.59	0.58	0.05712	0.00186	0.6155	0.02069	0.07826	0.00192	495.5	70.67	487	13	485.7	11.45	100.3
Z2056	36.49	115.39	0.32	0.05763	0.00343	0.6664	0.03895	0.08397	0.00247	515.5	125.88	518.5	23.73	519.8	14.69	99.7
Z2057	385.83	1418.37	0.27	0.05205</td												

Continued Table 1

Spot	Th conc	U conc	Th/U	$^{207}\text{Pb}/^{206}\text{Pb}$		$^{207}\text{Pb}/^{235}\text{U}$		$^{206}\text{Pb}/^{238}\text{U}$		$^{207}\text{Pb}/^{206}\text{Pb}$		$^{207}\text{Pb}/^{235}\text{U}$		$^{206}\text{Pb}/^{238}\text{U}$		Concor. (%)
				ppm	ppm	Ratio	1s	Ratio	1s	Ratio	1s	Age±1s (Ma)	Age±1s (Ma)	Age±1s (Ma)	Age±1s (Ma)	
SC1-2																
Z2075	114.42	182.36	0.63	0.05142	0.00263	0.28599	0.01448	0.04031	0.00107	259.7	113.22	255.4	11.44	254.8	6.6	100.2
Z2076	58.1	134.07	0.43	0.06067	0.00301	0.68285	0.03336	0.08158	0.00225	627.5	103.41	528.5	20.13	505.6	13.41	104.5
Z2077	433.49	555.28	0.78	0.05096	0.00174	0.26347	0.00921	0.03748	0.00091	239	77.01	237.5	7.4	237.2	5.62	100.1
Z2080	123.75	336.7	0.37	0.05292	0.00167	0.37385	0.01219	0.05121	0.00122	325.5	70.08	322.5	9.01	321.9	7.48	100.2
Z2081	166.34	283.25	0.59	0.05302	0.00167	0.37918	0.01231	0.05185	0.00124	329.4	69.78	326.4	9.06	325.9	7.59	100.2
Z2082	113.29	186.98	0.61	0.10682	0.00233	4.64114	0.11225	0.31498	0.0073	1745.9	39.45	1756.7	20.2	1765.2	35.81	98.9
Z2083	120.49	362.64	0.33	0.05386	0.00185	0.42236	0.01483	0.05686	0.00138	364.9	75.57	357.7	10.59	356.5	8.45	100.3
Z2084	351.92	520.54	0.68	0.05353	0.00135	0.41363	0.01119	0.05602	0.0013	351.4	56.16	351.5	8.04	351.4	7.96	100.0
Z2085	105.47	341.43	0.31	0.05296	0.00271	0.37552	0.01893	0.05142	0.00139	327	111.69	323.7	13.97	323.2	8.55	100.2
Z2086	94.37	181.23	0.52	0.05218	0.00198	0.33644	0.01291	0.04675	0.00115	293.4	84.04	294.5	9.81	294.5	7.08	100.0
Z2087	151.42	231.1	0.66	0.05643	0.00241	0.58779	0.02506	0.07553	0.00195	468.7	92.48	469.5	16.03	469.4	11.69	100.0
Z2088	29.43	47.63	0.62	0.05325	0.00427	0.39327	0.03103	0.05356	0.00162	339.3	171.85	336.8	22.61	336.3	9.89	100.1
Z2089	362.95	398.16	0.91	0.05591	0.00159	0.54984	0.01635	0.07132	0.00169	448.5	61.81	444.9	10.71	444.1	10.19	100.2
Z2090	115.67	181.88	0.64	0.05785	0.00319	0.66103	0.03592	0.08288	0.00231	523.8	116.69	515.2	21.96	513.3	13.78	100.4
Z2091	70.51	119.57	0.59	0.05147	0.00516	0.2966	0.02905	0.04179	0.00144	262	214.55	263.7	22.75	263.9	8.89	99.9
Z2092	142.15	98.78	1.44	0.05149	0.00595	0.28988	0.03281	0.04083	0.00147	262.9	245.39	258.5	25.83	258	9.08	100.2
Z2094	132.69	173.6	0.76	0.05258	0.00203	0.3609	0.01409	0.04979	0.00123	310.7	85.56	312.9	10.52	313.2	7.58	99.9
Z2095	406.6	413.42	0.98	0.05694	0.00153	0.61059	0.01737	0.07779	0.00184	488.7	58.92	483.9	10.95	482.9	11	100.2
Z2096	94.16	132.4	0.71	0.0514	0.00322	0.29387	0.01806	0.04148	0.00119	259	137.77	261.6	14.17	262	7.34	99.8
Z2097	174.15	185.45	0.94	0.053	0.00227	0.37573	0.0161	0.05144	0.00132	328.6	94.26	323.9	11.88	323.4	8.09	100.2
Z2098	311.43	318.3	0.98	0.05156	0.00226	0.29245	0.01282	0.04116	0.00105	265.8	97.47	260.5	10.07	260	6.53	100.2
Z2099	388.69	442.77	0.88	0.05291	0.00177	0.37657	0.01286	0.05164	0.00126	325	74.19	324.5	9.49	324.6	7.75	100.0
Z2100	86.15	210.15	0.41	0.05287	0.00237	0.37631	0.01685	0.05165	0.00134	323.3	98.65	324.3	12.43	324.6	8.18	99.9
Z2101	119.92	825.7	0.15	0.05702	0.00137	0.61949	0.01607	0.07884	0.00184	491.7	52.66	489.5	10.07	489.2	11.02	100.1
Z2102	97.02	98.5	0.98	0.05814	0.00224	0.69771	0.02708	0.08709	0.00221	534.7	82.54	537.4	16.2	538.3	13.09	99.8
Z2103	54.95	72.55	0.76	0.05322	0.00395	0.40196	0.02918	0.05482	0.00168	338.1	159.34	343.1	21.14	344	10.29	99.7
Z2104	128.31	217.97	0.59	0.05304	0.00224	0.38334	0.01619	0.05246	0.00135	330.4	92.89	329.5	11.88	329.6	8.26	100.0
Z2105	81.13	115.79	0.70	0.0537	0.00293	0.42593	0.02293	0.05757	0.0016	358.3	118.19	360.3	16.33	360.9	9.74	99.8
Z2106	133.2	82.3	1.62	0.05163	0.00369	0.29525	0.0206	0.04151	0.00127	269.1	156.01	262.7	16.15	262.2	7.84	100.2
Z2107	217.97	346.8	0.63	0.05416	0.00205	0.44311	0.01688	0.05939	0.0015	377.5	82.16	372.4	11.88	371.9	9.11	100.1
Z2108	315.48	538.51	0.59	0.05257	0.00174	0.3468	0.01176	0.0479	0.00118	310.3	73.7	302.3	8.87	301.6	7.24	100.2
Z2109	82.42	196.43	0.42	0.05732	0.00179	0.64698	0.02085	0.08196	0.00201	503.5	67.83	506.6	12.85	507.8	11.96	99.8
Z2110	317.92	354.04	0.90	0.05126	0.00209	0.28252	0.01157	0.04002	0.00102	252.6	91.23	252.7	9.16	253	6.31	99.9
Z2111	111.74	170.05	0.66	0.05692	0.00188	0.61585	0.02086	0.07857	0.00194	488	71.94	487.2	13.11	487.6	11.57	99.9
Z2112	58.5	87.87	0.67	0.05263	0.0029	0.36005	0.01958	0.04968	0.00136	312.9	120.42	312.3	14.62	312.6	8.38	99.9
Z2113	111.66	277.25	0.40	0.05156	0.00176	0.29859	0.01041	0.04206	0.00103	266.1	76.46	265.3	8.14	265.6	6.39	99.9
SC1-3																
Z3001	29.04	46.25	0.63	0.05454	0.00381	0.47309	0.03259	0.06288	0.00184	393.5	149.53	393.3	22.47	393.1	11.15	100.1
Z3002	52.15	153.76	0.34	0.08005	0.00199	2.07128	0.05577	0.18759	0.00449	1198.2	48.29	1139.4	18.44	1108.3	24.4	108.1
Z3003	435.31	653.77	0.67	0.05411	0.0014	0.44894	0.01248	0.06016	0.00143	375.3	57.1	376.5	8.74	376.6	8.67	100.0
Z3004	77.74	309.28	0.25	0.05219	0.00229	0.33078	0.01454	0.04595	0.00119	293.8	97.23	290.2	11.1	289.6	7.35	100.2
Z3005	54.03	123.23	0.44	0.05331	0.00216	0.39468	0.01618	0.05368	0.00135	342.1	88.93	337.8	11.78	337.1	8.27	100.2
Z3006	175.33	273.62	0.64	0.05231	0.0017	0.33292	0.01119	0.04615	0.00112	298.9	72.34	291.8	8.53	290.8	6.91	100.3
Z3007	375.37	729.27	0.51	0.05199	0.00127	0.31833	0.00845	0.0444	0.00104	285	377.5	302.3	8.87	301.6	7.24	100.2
Z3008	154.45	226.23	0.68	0.06601	0.00163	1.16459	0.0312	0.12793	0.00303	806.6	50.93	784.1	14.64	776.1	17.3	101.0
Z3009	237.08	121.32	1.95	0.07875	0.0021	2.22828	0.06327	0.20518	0.00498	1165.9	51.88	1190	19.9	1203.1	26.63	96.9
Z3010	159.25	297.82	0.53	0.05231	0.00187	0.33652	0.01227	0.04665	0.00116	299.1	79.36	294.5	9.32	293.9	7.11	100.2
Z3011	185.38	333.29	0.56	0.05222	0.0018	0.34124	0.01204	0.04739	0.00116	294.9	76.51	298.1	9.11	298.5	7.16	99.9
Z3012	57	112.94	0.50	0.05206	0.00268	0.31968	0.0164	0.04453	0.00118	288	113.59	281.7	12.61	280.9	7.26	100.3
Z3013	270.39	597.85	0.45	0.05535	0.00159	0.51878	0.01567	0.06798	0.00163	426	62.53	424.3	10.47	424	9.85	100.1
Z3015	73.42	132.62	0.55	0.05291	0.00277	0.38131	0.01975	0.05227	0.00142	324.7	114.39	328	14.52	328.5	8.71	99.8
Z3016	66.25	119.18	0.56	0.0744	0.00194	1.88413	0.05242	0.18367	0.0044	1052.5	51.55	1075.5	18.46	1087	23.97	96.8
Z3017	36.52	109.19	0.33	0.05202	0.00398	0.32247	0.02402	0.04496	0.00144	286.3	165.66	283.8	18.44	283.5	8.85	100.1
Z3018	196.14	483.18	0.41	0.06893	0.00147	1.44067	0.03444	0.1516	0.00351	896.5	43.47	906	14.33	910	19.66	99.6
Z3019	106.26	216.21	0.49	0.05201	0.00204	0.32187	0.01278	0.04489	0.00113	286						

Continued Table 1

Spot	Th conc	U conc	Th/U	$^{207}\text{Pb}/^{206}\text{Pb}$		$^{207}\text{Pb}/^{235}\text{U}$		$^{206}\text{Pb}/^{238}\text{U}$		$^{207}\text{Pb}/^{206}\text{Pb}$		$^{207}\text{Pb}/^{235}\text{U}$		$^{206}\text{Pb}/^{238}\text{U}$		Concor.
				Ratio	1s	Ratio	1s	Ratio	1s	Age±1s (Ma)	Age±1s (Ma)	Age±1s (Ma)	Age±1s (Ma)	(%)		
Z3037	215.74	284.88	0.76	0.05675	0.00198	0.61228	0.02169	0.07831	0.00193	481	75.78	485	13.66	486	11.57	99.8
Z3038	136.44	324.31	0.42	0.0524	0.00193	0.34113	0.0127	0.04725	0.00117	303	81.63	298	9.62	297.6	7.19	100.1
Z3039	183.51	276.03	0.66	0.06844	0.00173	1.37841	0.03728	0.14617	0.00345	881.9	51.54	879.8	15.92	879.5	19.4	100.0
Z3040	116.5	232.23	0.50	0.05209	0.00213	0.32269	0.01323	0.04496	0.00113	289.3	90.57	284	10.16	283.5	6.99	100.2
Z3041	32.75	71.16	0.46	0.05284	0.00345	0.37272	0.02397	0.0512	0.00144	321.9	141	321.7	17.73	321.9	8.81	99.9
Z3042	310.84	673.96	0.46	0.0558	0.00156	0.54629	0.01601	0.07106	0.00168	444.2	60.87	442.6	10.51	442.5	10.13	100.0
Z3043	35.28	55.97	0.63	0.05363	0.00359	0.41067	0.02697	0.05558	0.00162	355.5	143.95	349.4	19.41	348.7	9.87	100.2
Z3044	46.07	119.1	0.39	0.05178	0.00263	0.30579	0.01535	0.04286	0.00114	275.9	112.15	270.9	11.94	270.6	7.04	100.1
Z3045	144.98	273.27	0.53	0.05219	0.00177	0.33365	0.01154	0.0464	0.00112	293.8	75.38	292.3	8.79	292.4	6.93	100.0
Z3046	108.06	118.5	0.91	0.07341	0.00199	1.87556	0.05345	0.18547	0.00444	1025.2	53.78	1072.5	18.87	1096.8	24.17	93.5
Z3047	115.74	216.15	0.54	0.09624	0.00212	3.67211	0.08887	0.27698	0.00643	1552.4	40.76	1565.3	19.32	1576.1	32.47	98.5
Z3048	63.81	103.31	0.62	0.05348	0.00306	0.40619	0.02281	0.05514	0.00154	349.1	123.64	346.1	16.47	346	9.43	100.0
Z3049	937.12	1093.64	0.86	0.05595	0.00139	0.54675	0.01455	0.07095	0.00165	450	54.28	442.9	9.55	441.9	9.93	100.2
Z3050	60.42	164.06	0.37	0.05529	0.00217	0.51105	0.02017	0.0671	0.00169	424	85.23	419.2	13.56	418.7	10.22	100.1
Z3051	67.44	208.57	0.32	0.05196	0.00192	0.3251	0.01217	0.04542	0.00112	283.8	82.43	285.8	9.33	286.4	6.88	99.8
Z3052	190.06	304.07	0.63	0.05185	0.00178	0.31385	0.01094	0.04395	0.00107	278.7	76.48	277.2	8.46	277.3	6.59	100.0
Z3053	40.44	121.11	0.33	0.05176	0.00281	0.30897	0.01656	0.04334	0.00117	274.8	119.82	273.4	12.84	273.5	7.22	100.0
Z3054	207.05	100.94	2.05	0.07939	0.00205	2.15896	0.05919	0.19745	0.00468	1181.8	50.26	1167.9	19.02	1161.6	25.18	101.7
Z3055	28.26	75.85	0.37	0.0521	0.00335	0.32342	0.02052	0.04508	0.00124	289.7	140.31	284.5	15.75	284.2	7.66	100.1
Z3056	79.34	107.08	0.74	0.05408	0.00317	0.44274	0.02541	0.05945	0.0017	374.1	126.43	372.2	17.88	372.3	10.34	100.0
Z3057	63.74	155.81	0.41	0.10819	0.00235	4.7794	0.11407	0.32076	0.00742	1769.1	39.17	1781.3	20.04	1793.5	36.23	98.6
Z3058	320.74	703.52	0.46	0.05204	0.00182	0.32298	0.01145	0.04507	0.0011	287.2	77.94	284.2	8.79	284.2	6.79	100.0
Z3059	57.61	153.38	0.38	0.05233	0.00208	0.34979	0.01844	0.04853	0.00132	300	117.57	304.6	13.87	305.5	8.12	99.7
Z3060	62.07	357.99	0.17	0.05213	0.00206	0.3364	0.01337	0.04686	0.00117	291	87.87	294.4	10.16	295.2	7.19	99.7
Z3061	81.84	146.71	0.56	0.05301	0.00264	0.38977	0.01938	0.05334	0.00142	329.1	109.02	334.2	14.16	335	8.71	99.8
Z3062	51.82	121.97	0.42	0.05182	0.00287	0.31573	0.01735	0.04442	0.00121	277.5	122.59	278.6	13.39	278.8	7.49	99.9
Z3063	103.92	172.04	0.60	0.05345	0.00205	0.41084	0.01608	0.05576	0.0014	347.8	84.34	349.5	11.57	349.8	8.52	99.9
Z3064	159.37	218.06	0.73	0.05335	0.00203	0.39261	0.01703	0.05338	0.00139	343.7	94.6	336.3	12.42	335.3	8.49	100.3
Z3065	161.23	547.45	0.29	0.05212	0.00141	0.32282	0.00936	0.04493	0.00107	290.5	60.72	284.1	7.19	283.3	6.61	100.3
Z3066	71.76	170.75	0.42	0.05674	0.00285	0.59779	0.0298	0.07643	0.0021	480.7	107.89	475.8	18.94	474.8	12.56	100.2
Z3067	58.84	118.48	0.50	0.05181	0.00296	0.30832	0.01734	0.04317	0.00122	277.2	125.64	272.9	13.46	272.4	7.52	100.2
Z3068	132.96	229.99	0.58	0.05226	0.00223	0.33382	0.01434	0.04634	0.00119	296.7	94.57	292.5	10.92	292	7.35	100.2
Z3069	186.68	445.67	0.42	0.05278	0.00159	0.37072	0.01171	0.05095	0.00123	319.3	67.06	320.2	8.68	320.4	7.55	99.9
Z3071	67.51	134.3	0.50	0.05195	0.0026	0.32209	0.0161	0.04498	0.00118	283.1	110.53	283.5	12.36	283.6	7.3	100.0
Z3072	300.68	593.95	0.51	0.05196	0.0014	0.32284	0.0093	0.04507	0.00107	283.8	60.42	284.1	7.14	284.2	6.61	100.0
Z3073	291.93	516.37	0.57	0.05203	0.00146	0.31914	0.00947	0.0445	0.00106	286.6	62.65	281.2	7.29	280.6	6.56	100.2
Z3074	259.88	653.57	0.40	0.05212	0.00158	0.33336	0.0106	0.04639	0.00112	290.8	67.85	292.1	8.07	292.3	6.9	99.9
Z3076	13.39	51.62	0.26	0.07867	0.00252	2.16255	0.07191	0.1994	0.00504	1163.9	62.29	1169.1	23.09	1172.1	27.08	99.3
Z3077	50.57	111.5	0.45	0.05317	0.00292	0.38789	0.02111	0.05292	0.00144	336.1	119.48	332.8	15.44	332.4	8.85	100.1
Z3078	105.82	302.88	0.35	0.05172	0.00234	0.30343	0.01372	0.04256	0.00112	273	100.54	269.1	10.69	268.7	6.92	100.1
Z3079	297.51	725.37	0.41	0.05186	0.00132	0.31852	0.00875	0.04455	0.00105	279.3	57.24	280.8	6.74	281	6.48	99.9
Z3080	187.08	372.73	0.50	0.05637	0.00143	0.57766	0.01578	0.07434	0.00176	466.1	55.65	463	10.16	462.3	10.54	100.2
Z3081	205.61	471.9	0.44	0.05258	0.00197	0.35989	0.01367	0.04965	0.00125	310.8	83.04	312.1	10.21	312.4	7.65	99.9
Z3082	31.73	57.34	0.55	0.05374	0.00383	0.4122	0.02875	0.05564	0.00171	360	153.15	350.5	20.67	349.1	10.47	100.4
Z3083	300.16	311.77	0.96	0.05211	0.00181	0.33399	0.01194	0.0465	0.00113	290.1	77.36	292.6	9.09	293	6.99	99.9
Z3084	147.85	178.08	0.83	0.08938	0.00199	3.12845	0.07736	0.25388	0.00596	1412.3	41.88	1439.7	19.03	1458.5	30.66	96.8
Z3085	125.21	265.09	0.47	0.05209	0.00177	0.32255	0.01126	0.04492	0.00111	289.2	75.58	283.9	8.64	283.3	6.77	100.2
Z3086	55.81	117.88	0.47	0.05205	0.0026	0.33191	0.01652	0.04625	0.00121	287.6	110.18	291	12.59	291.5	7.48	99.8
Z3087	135	311.93	0.43	0.05247	0.00175	0.35016	0.01206	0.0484	0.00118	306.1	74.29	304.8	9.07	304.7	7.27	100.0
Z3088	168.08	208.32	0.81	0.05211	0.00211	0.33222	0.0136	0.04625	0.00117	290.2	89.85	291.3	10.36	291.4	7.18	100.0
Z3089	69.93	125.27	0.56	0.05243	0.0024	0.34861	0.01599	0.04822	0.00125	304.4	101.2	303.7	12.04	303.6	7.68	100.0
Z3090	95.31	173.61	0.55	0.05402	0.00216	0.44128	0.01778	0.05925	0.0015	371.7	86.85	371.2	12.52	371.1	9.16	100.0
Z3091	22.31	62.88	0.35	0.05216	0.00432	0.3306	0.02703	0.04598	0.00135	292.2	178.01	290	20.63	289.8	8.32	100.1
Z3092	122.87	228.57	0.54	0.05256	0.00231	0.35661	0.01574	0.04922	0.00125	309.6	96.94	309.7	11.78	309.7	7.69	100.0
Z3093	64.86	159.64	0.41	0.05214	0.0026	0.33774	0.01677	0.04698	0.00124	291.5	109.99					

Continued Table 1

Spot	Th conc	U conc	Th/U	$^{207}\text{Pb}/^{206}\text{Pb}$		$^{207}\text{Pb}/^{235}\text{U}$		$^{206}\text{Pb}/^{238}\text{U}$		$^{207}\text{Pb}/^{206}\text{Pb}$		$^{207}\text{Pb}/^{235}\text{U}$		$^{206}\text{Pb}/^{238}\text{U}$		Concor. (%)
				Ratio	1s	Ratio	1s	Ratio	1s	Age±1s (Ma)	Age±1s (Ma)	Age±1s (Ma)	Concor. (%)	Concor. (%)	Concor. (%)	
Z4003	128.76	188.82	0.68	0.05222	0.00242	0.33433	0.01554	0.04645	0.00121	295.1	102.29	292.9	11.83	292.7	7.45	100.1
Z4004	220.62	343.78	0.64	0.0574	0.00228	0.62576	0.02525	0.07911	0.00202	506.5	85.42	493.4	15.77	490.8	12.08	100.5
Z4007	86.59	149.27	0.58	0.0542	0.00519	0.4419	0.04136	0.05916	0.00206	379.1	202.21	371.6	29.13	370.5	12.52	100.3
Z4008	53.2	54.2	0.98	0.05514	0.00388	0.51109	0.03562	0.06726	0.00194	417.6	150	419.2	23.93	419.6	11.7	99.9
Z4009	31.59	38.88	0.81	0.0523	0.00658	0.33976	0.04239	0.04714	0.00149	298.5	264.08	297	32.12	296.9	9.19	100.0
Z4010	20.16	48.56	0.42	0.05519	0.00388	0.51746	0.03594	0.06803	0.00201	419.7	149.94	423.5	24.05	424.3	12.11	99.8
Z4011	47.04	68.73	0.68	0.05338	0.00383	0.39684	0.02826	0.05394	0.00154	344.8	154.38	339.4	20.54	338.7	9.44	100.2
Z4012	144.77	224.36	0.65	0.05325	0.00239	0.3924	0.01778	0.05347	0.00138	339.3	98.34	336.1	12.96	335.8	8.45	100.1
Z4013	45.74	172.79	0.26	0.06988	0.00236	1.47665	0.05172	0.15333	0.00387	924.7	67.82	920.9	21.2	919.6	21.66	100.1
Z4014	192.93	301.26	0.64	0.05237	0.00197	0.34318	0.01325	0.04754	0.00118	301.6	83.3	299.6	10.01	299.4	7.26	100.1
Z4015	44.25	65.94	0.67	0.05184	0.00461	0.30794	0.0269	0.0431	0.00138	278.3	191.03	272.6	20.88	272	8.55	100.2
Z4016	15.02	62.68	0.24	0.05611	0.00342	0.56168	0.03399	0.07263	0.00205	456.3	130.22	452.6	22.1	452	12.32	100.1
Z4017	45.8	110.52	0.41	0.05138	0.00737	0.29401	0.04108	0.04152	0.00181	257.7	299.94	261.7	32.23	262.2	11.22	99.8
Z4018	44.17	160.27	0.28	0.19376	0.00431	14.18257	0.3598	0.53108	0.01266	2774.3	36.05	2762	24.06	2746	53.29	101.0
Z4019	86.73	194.86	0.45	0.10401	0.00245	4.11295	0.10846	0.28689	0.00683	1696.9	42.82	1656.9	21.54	1626	34.2	104.4
Z4020	66.52	79.96	0.83	0.05574	0.00725	0.5506	0.07008	0.07166	0.0029	441.9	266.18	445.4	45.89	446.2	17.43	99.8
Z4022	180.75	173.22	1.04	0.05349	0.00264	0.40979	0.02029	0.05558	0.00146	349.7	107.47	348.7	14.62	348.7	8.94	100.0
Z4023	541.8	376.02	1.44	0.05246	0.00199	0.34138	0.01326	0.04721	0.00118	305.4	84.02	298.2	10.04	297.4	7.28	100.3
Z4024	119.32	319.1	0.37	0.05549	0.00217	0.52601	0.02097	0.06877	0.00175	431.9	84.7	429.2	13.95	428.7	10.56	100.1
Z4025	189.45	222.79	0.85	0.05517	0.00242	0.51218	0.02272	0.06735	0.00175	419.1	94.98	419.9	15.26	420.2	10.6	99.9
Z4026	107.25	282.67	0.38	0.05418	0.00236	0.44191	0.01945	0.05917	0.00154	378.5	94.56	371.6	13.69	370.6	9.39	100.3
Z4029	312.95	446.88	0.70	0.05732	0.00189	0.62904	0.02163	0.07962	0.00197	503.4	71.32	495.5	13.48	493.8	11.77	100.3
Z4030	42.9	307.58	0.14	0.09937	0.00224	3.98956	0.10212	0.29127	0.00689	1612.3	41.45	1632.1	20.78	1647.9	34.41	97.8
Z4031	465.38	484.55	0.96	0.05449	0.00189	0.46309	0.01667	0.06166	0.00154	391.1	75.38	386.4	11.57	385.7	9.33	100.2
Z4032	76.4	171.03	0.45	0.05663	0.00212	0.58987	0.02267	0.07557	0.00191	476.3	81.31	470.8	14.48	469.7	11.43	100.2
Z4033	118.51	287.43	0.41	0.05564	0.00194	0.53178	0.0192	0.06934	0.00173	437.6	75.65	433	12.73	432.2	10.42	100.2
Z4034	60.98	110.96	0.55	0.05617	0.0024	0.57766	0.0251	0.07461	0.00191	458.8	92.38	463	16.15	463.9	11.49	99.8
Z4035	87.54	155.56	0.56	0.05325	0.00237	0.3974	0.01791	0.05415	0.00139	339.2	97.44	339.8	13.01	339.9	8.53	100.0
Z4036	38.55	512.26	0.08	0.09696	0.00211	3.54209	0.08836	0.26503	0.00623	1566.4	40.17	1536.7	19.75	1515.5	31.76	103.4
Z4037	147.42	221.83	0.66	0.05535	0.0024	0.5061	0.02221	0.06634	0.00174	426	94.05	415.8	14.97	414.1	10.53	100.4
Z4038	197.22	278.02	0.71	0.05532	0.00174	0.5041	0.01675	0.06611	0.00162	425.1	68.3	414.5	11.31	412.7	9.81	100.4
Z4039	80.71	373.82	0.22	0.05516	0.00234	0.50426	0.02168	0.06632	0.00173	418.6	91.86	414.6	14.64	414	10.46	100.1
Z4040	231.03	310	0.75	0.05535	0.00234	0.52073	0.02226	0.06826	0.00178	426	91.43	425.6	14.86	425.6	10.76	100.0
Z4041	114.15	251.84	0.45	0.05595	0.00166	0.55956	0.0177	0.07255	0.00176	450.2	64.53	451.2	11.52	451.5	10.58	99.9
Z4042	42.83	54.92	0.78	0.05461	0.00542	0.47753	0.04609	0.06344	0.00236	396.2	208.25	396.4	31.68	396.5	14.29	100.0
Z4043	88.08	135.18	0.65	0.05622	0.00293	0.56663	0.02949	0.07312	0.00202	460.3	112.44	455.8	19.11	454.9	12.14	100.2
Z4044	40.98	111.95	0.37	0.0687	0.00239	1.3834	0.05002	0.14609	0.00373	889.7	70.38	889.1	21.31	879	21	100.3
Z4045	331.84	475.31	0.70	0.05294	0.00168	0.38418	0.01286	0.05265	0.00129	326	70.66	330.1	9.44	330.8	7.92	99.8
Z4046	0.56	89.57	0.01	0.0567	0.00314	0.60992	0.03363	0.07805	0.00218	479	118.52	483.5	21.21	484.5	13.04	99.8
Z4047	99.31	149.28	0.67	0.05467	0.00259	0.47396	0.0226	0.0629	0.00167	398.6	102.35	393.9	15.57	393.2	10.16	100.2
Z4048	61.6	124.72	0.49	0.0551	0.00246	0.50516	0.02282	0.06651	0.00173	416.3	96.37	415.2	15.39	415.1	10.46	100.0
Z4049	113.12	192.15	0.59	0.05468	0.00197	0.47387	0.01769	0.06287	0.00157	399.2	77.98	393.9	12.19	393.1	9.52	100.2
Z4050	142.91	230.74	0.62	0.05274	0.00238	0.36588	0.01672	0.05033	0.00103	317.5	99.28	316.6	12.43	316.6	8.01	100.0
Z4051	118.43	205.66	0.58	0.05444	0.00287	0.45913	0.02404	0.06119	0.00171	389.1	113.61	383.6	16.73	382.9	10.39	100.2
Z4052	0.7	54.63	0.01	0.07957	0.00269	2.14553	0.0757	0.19564	0.00504	1186.2	65.38	1163.6	24.44	1151.8	27.17	103.0
Z4053	67.87	292.56	0.23	0.069	0.00166	1.3382	0.03603	0.14071	0.00337	898.6	48.9	862.4	15.65	848.7	19.03	101.6
Z4054	71.02	85.94	0.83	0.05235	0.00355	0.34871	0.02356	0.04832	0.00135	300.8	147.44	303.7	17.74	304.2	8.32	99.8
Z4055	250.28	330.48	0.76	0.05609	0.00162	0.56243	0.01747	0.07275	0.00177	455.6	63.09	453.1	11.36	452.7	10.64	100.1
Z4056	54.44	176.94	0.31	0.05731	0.00307	0.63941	0.03403	0.08094	0.00231	503.1	114.26	501.9	21.08	501.7	13.77	100.0
Z4057	344.68	559.57	0.62	0.05408	0.00189	0.43327	0.0157	0.05812	0.00146	374.3	76.56	365.5	11.12	364.2	8.91	100.4
Z4058	219.5	242.27	0.91	0.05354	0.00271	0.40712	0.02062	0.05517	0.00151	351.5	109.94	346.8	14.88	346.2	9.22	100.2
Z4059	84.02	125.23	0.67	0.05137	0.00287	0.28152	0.01561	0.03976	0.00111	257.5	123.21	251.9	12.37	251.3	6.87	100.2
Z4060	124.3	148.06	0.84	0.05506	0.00396	0.49649	0.03501	0.06542	0.00206	414.6	153.17	409.3	23.75	408.5	12.48	100.2
Z4061	139.49	368.65	0.38	0.05602	0.0025	0.54347	0.02448	0.07042	0.00184	452.9	96.44	440.7	16.1	438.7	11.07	100.5
Z4062	63.04	107.3	0.59	0.05517	0.00											

Continued Table 1

Spot	Th conc	U conc	Th/U	$^{207}\text{Pb}/^{206}\text{Pb}$		$^{207}\text{Pb}/^{235}\text{U}$		$^{206}\text{Pb}/^{238}\text{U}$		$^{207}\text{Pb}/^{206}\text{Pb}$		$^{207}\text{Pb}/^{235}\text{U}$		$^{206}\text{Pb}/^{238}\text{U}$		Concor.
				ppm	ppm	Ratio	1s	Ratio	1s	Ratio	1s	Age±1s (Ma)	Age±1s (Ma)	Age±1s (Ma)	(%)	
SC1-2																
Z4084	400.78	427.14	0.94	0.05295	0.00157	0.37836	0.01194	0.0518	0.00126	326.5	65.99	325.8	8.8	325.6	7.75	100.1
Z4085	151.97	337.97	0.45	0.05554	0.00158	0.52055	0.01584	0.06795	0.00166	433.6	61.79	425.5	10.58	423.8	10.01	100.4
Z4086	283.54	393.87	0.72	0.05389	0.00168	0.43384	0.01424	0.05836	0.00145	366.4	68.68	365.9	10.08	365.6	8.8	100.1
Z4087	232.83	436.34	0.53	0.05565	0.00174	0.54074	0.01772	0.07044	0.00175	438.2	67.82	438.9	11.68	438.8	10.55	100.0
Z4088	199.23	222.59	0.90	0.05070	0.00242	0.50277	0.02221	0.06618	0.00176	415	94.86	413.6	15.01	413.1	10.66	100.1
Z4089	100.04	196.29	0.51	0.05622	0.00198	0.58007	0.0211	0.0748	0.0019	460.4	76.39	464.5	13.56	465	11.37	99.9
Z4090	46.67	93.54	0.50	0.05263	0.00283	0.35703	0.0192	0.04918	0.00133	312.9	117.66	310	14.36	309.5	8.19	100.2
Z4091	214.47	228.86	0.94	0.05256	0.00253	0.35862	0.0172	0.04947	0.00136	309.9	105.92	311.2	12.86	311.3	8.35	100.0
Z4092	142.21	245.78	0.58	0.05417	0.00231	0.44837	0.01928	0.06002	0.00159	377.8	92.54	376.1	13.52	375.7	9.68	100.1
Z4093	55.73	73.33	0.76	0.04995	0.00305	0.37905	0.0231	0.05503	0.00153	192.5	136.25	326.3	17.01	345.3	9.33	94.5
Z4094	37.5	67.22	0.56	0.05656	0.00463	0.5944	0.04773	0.0762	0.00251	473.8	172.26	473.7	30.4	473.4	15.01	100.1
Z4095	161.8	239.24	0.68	0.05286	0.00189	0.36778	0.01354	0.05046	0.00129	322.6	79.35	318	10.05	317.4	7.9	100.2
Z4096	30.76	55.8	0.55	0.05445	0.00388	0.46595	0.03269	0.06206	0.00191	389.8	151.98	388.4	22.65	388.1	11.6	100.1
Z4097	72.68	168.99	0.43	0.06874	0.0017	1.47474	0.04005	0.15564	0.00382	890.8	50.18	920.1	16.43	932.5	21.29	98.7
Z4098	117.01	245.82	0.48	0.05628	0.00175	0.57241	0.0187	0.07379	0.00186	462.5	67.99	459.6	12.07	459	11.16	100.1
Z4099	78.56	128.19	0.61	0.05389	0.00212	0.43977	0.01767	0.05921	0.00154	366.3	86.29	370.1	12.46	370.8	9.37	99.8
Z4100	134.72	272.75	0.49	0.05347	0.0025	0.4022	0.01882	0.05458	0.00149	348.5	102.3	343.2	13.63	342.6	9.14	100.2
Z4101	121.87	185.22	0.66	0.05376	0.00212	0.42907	0.01715	0.05792	0.00152	360.8	86.25	362.5	12.19	362.9	9.27	99.9
Z4102	99.65	158.66	0.63	0.05259	0.00235	0.35332	0.01587	0.04875	0.00131	311.3	98.76	307.2	11.91	306.9	8.07	100.1
Z4103	79.21	166.31	0.48	0.05555	0.00196	0.52745	0.01915	0.06892	0.00177	434.3	76.57	430.1	12.73	429.6	10.69	100.1
Z4104	67.88	203.4	0.33	0.05662	0.00295	0.60033	0.03094	0.07697	0.00223	476.1	111.98	477.4	19.63	478	13.34	99.9
Z4105	30.58	116.01	0.26	0.05525	0.00287	0.52455	0.02691	0.06893	0.00199	422	111.47	428.2	17.92	429.7	11.98	99.7
Z4106	18.18	64.72	0.28	0.13388	0.0032	7.60821	0.20182	0.41261	0.01057	2149.5	41.18	2185.8	23.81	2226.8	48.22	96.5
Z4107	61.01	147.18	0.41	0.05494	0.00185	0.60063	0.021	0.07939	0.00203	409.6	73.14	477.6	13.32	492.5	12.13	97.0

rocks, granitic plutons, and Precambrian rocks (Hu et al., 2000; Huang et al., 2015; Wang et al., 2017). Nevertheless, the possibility that partial contribution from the Jueluotag could not be ruled out because the Jueluotag is dominated by Late Paleozoic volcanic-sedimentary rocks, with a small quantity of Ordovician to Devonian volcanic-sedimentary rocks and Paleozoic intrusive rocks (Xiao et al., 2004; Han and Zhao, 2018; Huang et al., 2018). By contrast, the age spectrum of sample SC1-3 from Middle Triassic shows a prominent Early Permian age peak and an obvious reduction of the Pre-Carboniferous age signal, implying increased contribution from the Jueluotag and decreased contribution from the Central Tianshan subunit. The age spectrum of sample SC1-2 from the Upper Triassic exhibits a marked Late Paleozoic age population as well, while it defines a Late Carboniferous major peak and an early Permian minor peak. The age peak shift between sample SC1-3 and sample SC1-2 implies that persistent unroofing of the Jueluotag brought deeper Carboniferous rocks to the surface. Notably, the sample SC1-2 contains several zircon grains with Triassic age. Because the zircon grains with Triassic age show igneous origin in CL images (Fig. 4a) and there is no volcanic activity in Turpan-Hami Basin and its periphery during Triassic, we infer that the occurrence of zircon grains with Triassic age in the Upper Triassic sample SC1-2 indicates that the Indosinian plutons in the Eastern Tianshan might have been experienced a rapid emplacement-exhumation process. This inference is supported by recent low temperature thermochronological studies (Jolivet et al., 2010; Yin et al., 2018), which also revealed an Indosinian cooling and exhumation event.

Quantitatively, the low P values ( $<0.05$ ) for K-S test (Table 2) between the Lower Triassic sample SC1-4 and the Middle-Upper Triassic sample SC1-3 and sample SC1-

2 imply that there is 95% confidence that it is likely that the Lower Triassic and Middle-Upper Triassic samples come from different populations, which is also supported by the cumulative probability plot because they show significantly different cumulative probability curves (Fig. 6b). On the contrary, the high P value ( $>0.05$ ) (Table 1) and similar cumulative probability curves (Fig. 6b) between the Middle Triassic sample SC1-3 and Upper Triassic sample SC1-2 indicates that they have a similar provenance despite an age peak shift between them. Additionally, in the MDS diagram (Fig. 6c) the Lower Triassic sample SC1-4 shows a close relationship with the Central Tianshan, while the Middle-Upper Triassic sample SC1-3 and sample SC1-2 show a high similarity with the Jueluotag.

Collectively, we suggest that zircon grains in the Lower Triassic sample SC1-4 were mainly sourced from the Central Tianshan, and the Jueluotag act as a minor provenance. By contrast, the Late Paleozoic rocks in the Jueluotag act as the main provenance for the Middle-Upper Triassic sample SC1-3 and sample SC1-2, and the Central Tianshan act as a minor provenance. Furthermore, zircon grains in the Middle Triassic sample SC1-3 were mainly sourced from the Permian rocks in the Jueluotag, while Indosinian rapid exhumation brought deeper Carboniferous rocks of the Jueluotag as an important age population for the Upper Triassic sample SC1-2.

## 5.2 Genesis of the Permian-Triassic unconformity in the Eastern Tianshan and its periphery

The Permian-Triassic unconformity has been widely recognized throughout the Eastern Tianshan and its periphery (Greene et al., 2001; Su et al., 2006; Bai et al., 2010; Liao et al., 2011). However, the genesis of the Permian-Triassic unconformity is still in dispute (Greene et al., 2001; Liu et al., 2013; Liu et al., 2017; Ma et al.,

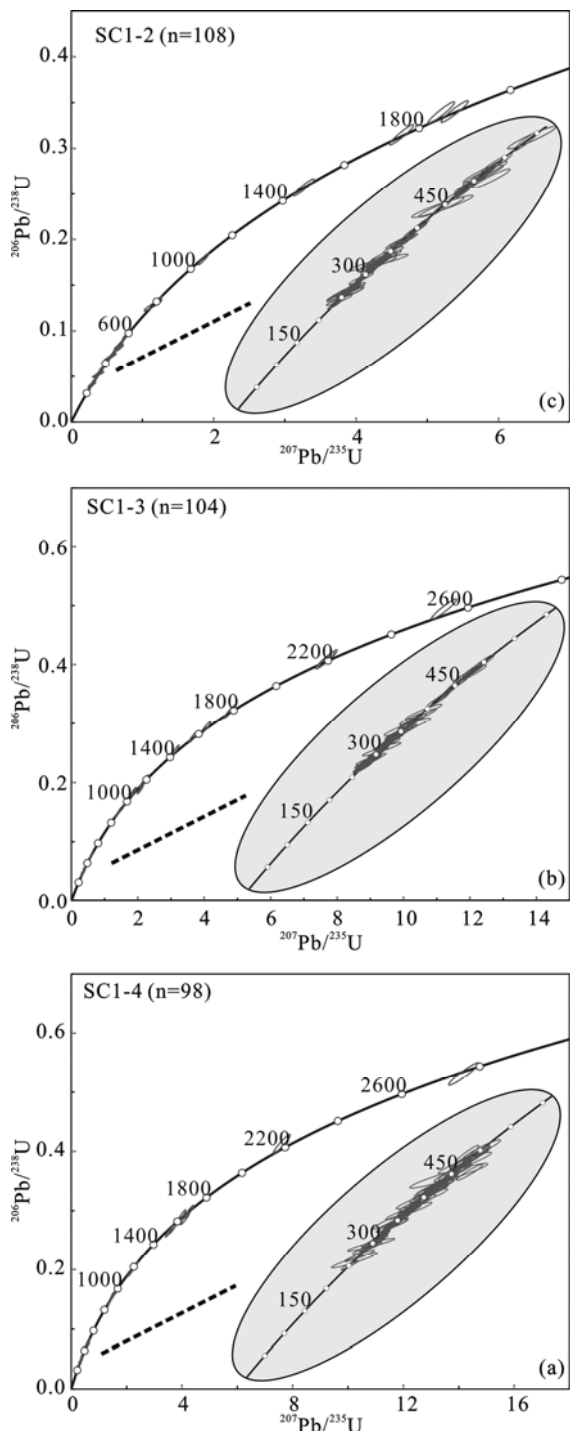


Fig. 5. U-Pb concordia diagrams showing the results of LA-ICP-MS analyses.

2018). Traditionally, there are three different hypotheses regarding its genesis, including 1) the Permian-Triassic unconformity is a product of the final closure of the North Tian Shan Ocean (Xiao et al., 2008); 2) the Permian-Triassic unconformity is related to post-rift on-lap deposition in a post-collisional extensional regime (Su et al., 2006; Liu et al., 2013); and 3) the Permian-Triassic unconformity is related to Late Permian tectonic contraction and inversion (Greene et al., 2001, 2005;

**Table 2** P values obtained from the Kolmogorov-Smirnov (K-S) test using cumulative age distribution curves

Sample ID	SC1-2	SC1-3	SC1-4
SC1-2	/	0.107	0.000
SC1-3	0.107	/	0.000
SC1-4	0.000	0.000	/

To be 95% confident that two populations are not statistically different, the P value must exceed 0.05.

Zhang et al., 2019b). Recent studies have demonstrated that the North Tian Shan Ocean has been closed prior to Permian (Han et al., 2010; Zhang et al., 2016), and the Eastern Tianshan and its periphery was in an intra-continental setting in the Permian-Triassic. Thus, the hypothesis 1 could be ruled out. Additionally, more evidence has been found to support to the Late Permian tectonic contraction and inversion (Greene et al., 2001; Yang et al., 2009; Jiang et al., 2015; Wang et al., 2018a; Zhang et al., 2019b), and therefore the hypothesis 3 rather than the hypothesis 2 seems the best interpretation. However, Liu et al. (2017) proposed that the Permian-Triassic unconformity is generated by an increasingly arid climate rather than tectonic uplift based mainly on no significant changes in the source-to-sink system from the Late Permian to the Triassic at limited outcrop sections. This again led to debate about the genesis of the Permian-Triassic unconformity (Ma et al., 2018). It is noticeable that most of these conclusions have been obtained based on outcrop sections along the piedmonts (Greene et al., 2005; Liu et al., 2013; Liu et al., 2017), whereas subsurface and intrabasinal data remain limited. Here we synthesize our new subsurface data and previously published subsurface data to reassess the genesis of the Permian-Triassic unconformity in the Eastern Tianshan and its periphery.

Zhang et al. (2019b) recently conducted a detrital zircon U-Pb geochronological study on Permian samples LN1-2 (Middle Permian), LN1-1 (Lower Permian), and LN1-3 (Lower Permian) collected from the Well LN1 in the southern Turpan-Hami Basin, indicating that the Permian sediments were mainly sourced from the Jueluotag. By contrast, our detrital zircon U-Pb geochronological study on the Triassic samples collected from the Well SC1 in the southern Turpan-Hami Basin suggests that the Triassic sediments were sourced from the Jueluotag and the Central Tianshan subunit. Therefore, subsurface data from the southern Turpan-Hami Basin suggest that there are significant changes in the source-to-sink system from the Permian to the Triassic (Fig. 7). Additionally, subsurface geological study (Jiang et al., 2015) in the Turpan-Hami Basin revealed that there was a compression and tectonic inversion event in the Turfan-Hami basin after the Middle Permian, which caused differential absence of the Upper Permian strata and erosion of the Middle Permian strata. Furthermore, Ma et al. (2018) conducted a comprehensive anatomy of the Permian-Triassic unconformity in the Eastern Tianshan and its periphery using seismic section and borehole data from the Chaiwopu Basin, and their data suggested that the Chaiwopu Basin experienced Late Permian-Early Triassic accelerated exhumation in a contractional setting and the Permian-Triassic

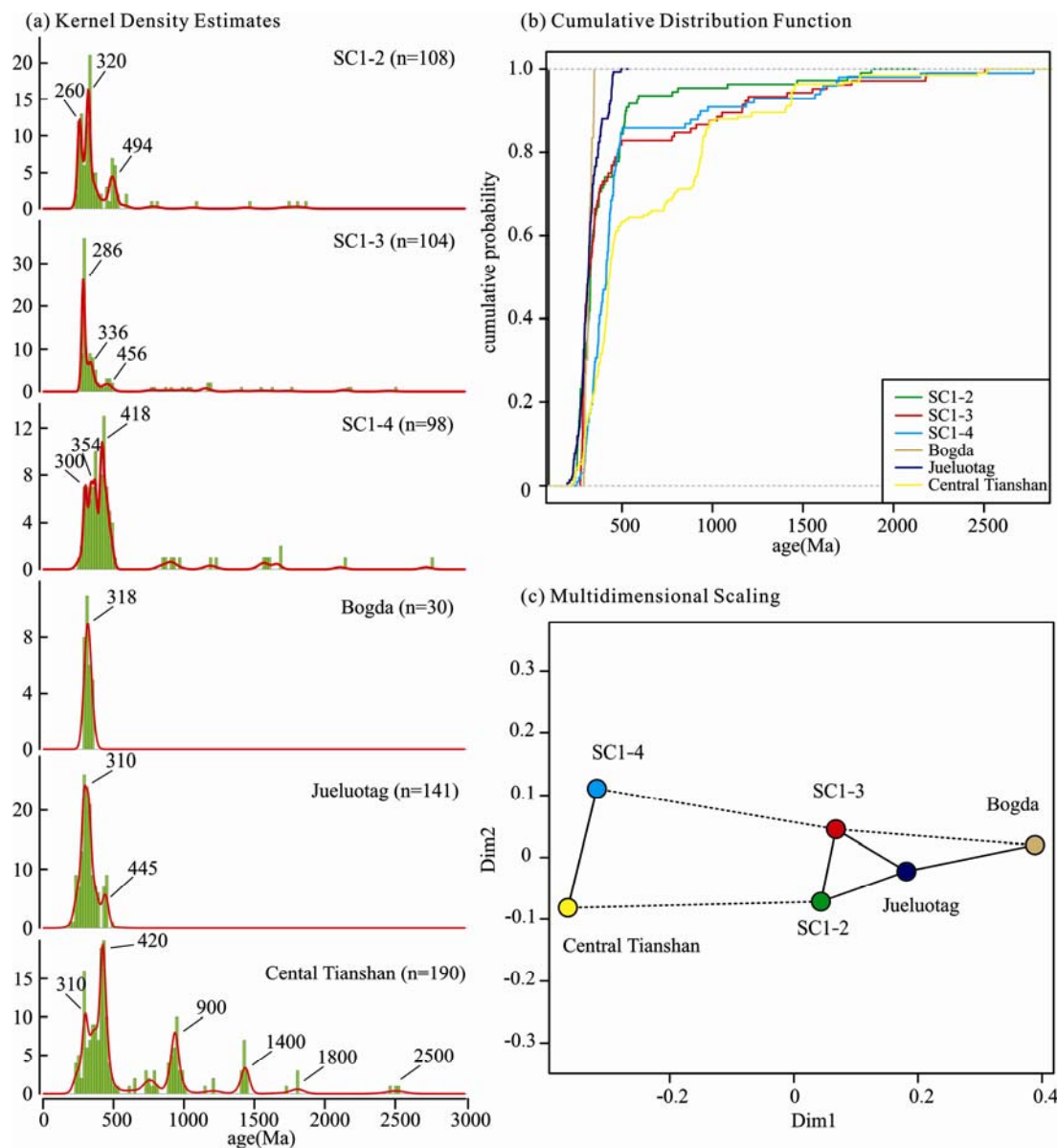


Fig. 6. (a) Kernel density estimate (KDE) diagrams, (b) cumulative probability plot (CPP), and (c) multidimensional scaling (MDS) plot of zircon U-Pb ages for the Triassic samples in this study and their potential sources. MDS plot groups the samples with similar age spectra, with solid and dashed lines marking the closest and the second closest neighbors, respectively. Data source: the Bogda from Wali et al. (2018); the Jueluotag modified from Huang et al. (2018); and the Central Tianshan supplemented from He et al. (2018). The data were plotted using IsoplotR (Vermeesch 2018).

unconformity is of syntectonic genesis. Putting all these together, we suggest that the Permian-Triassic unconformity in the Eastern Tianshan and its periphery is generated by the coeval tectonic contraction and inversion rather than an increasingly arid climate.

### 5.3 Implications for Indosinian tectonic reactivation in the Eastern Tianshan

The present Tianshan was traditionally considered to have resulted from the reactivation of the Paleozoic orogen induced by the Cenozoic Indo-Eurasia convergence (Tapponnier and Molnar, 1979; Windley et al., 1990; Hendrix et al., 1994; Dumitru et al., 2001;

Jolivet et al., 2010; Tian et al., 2016). A growing body of evidence (Chen et al., 2011, 2015; Tang et al., 2014, 2015, Yang et al., 2015, 2017; Yang W et al., 2017; Ji et al., 2018), however, suggests that the Eastern Tianshan and its periphery was initially reactivated during the Mesozoic. Specially, several studies furtherly demonstrated that strong tectonic activity occurred at the Late Mesozoic (Dumitru et al., 2001; Jolivet et al., 2010; Tang et al., 2014; Wang et al., 2015), while the Early Mesozoic was considered a period of relative tectonic quiescence (Li and Peng, 2013; Tang et al., 2014; Wang et al., 2016; Zhu et al., 2017; Wang et al., 2018b). In fact, Triassic magmatism (Zhang et al., 2005; Zhang et al., 2017a; Zhao H G et al.,

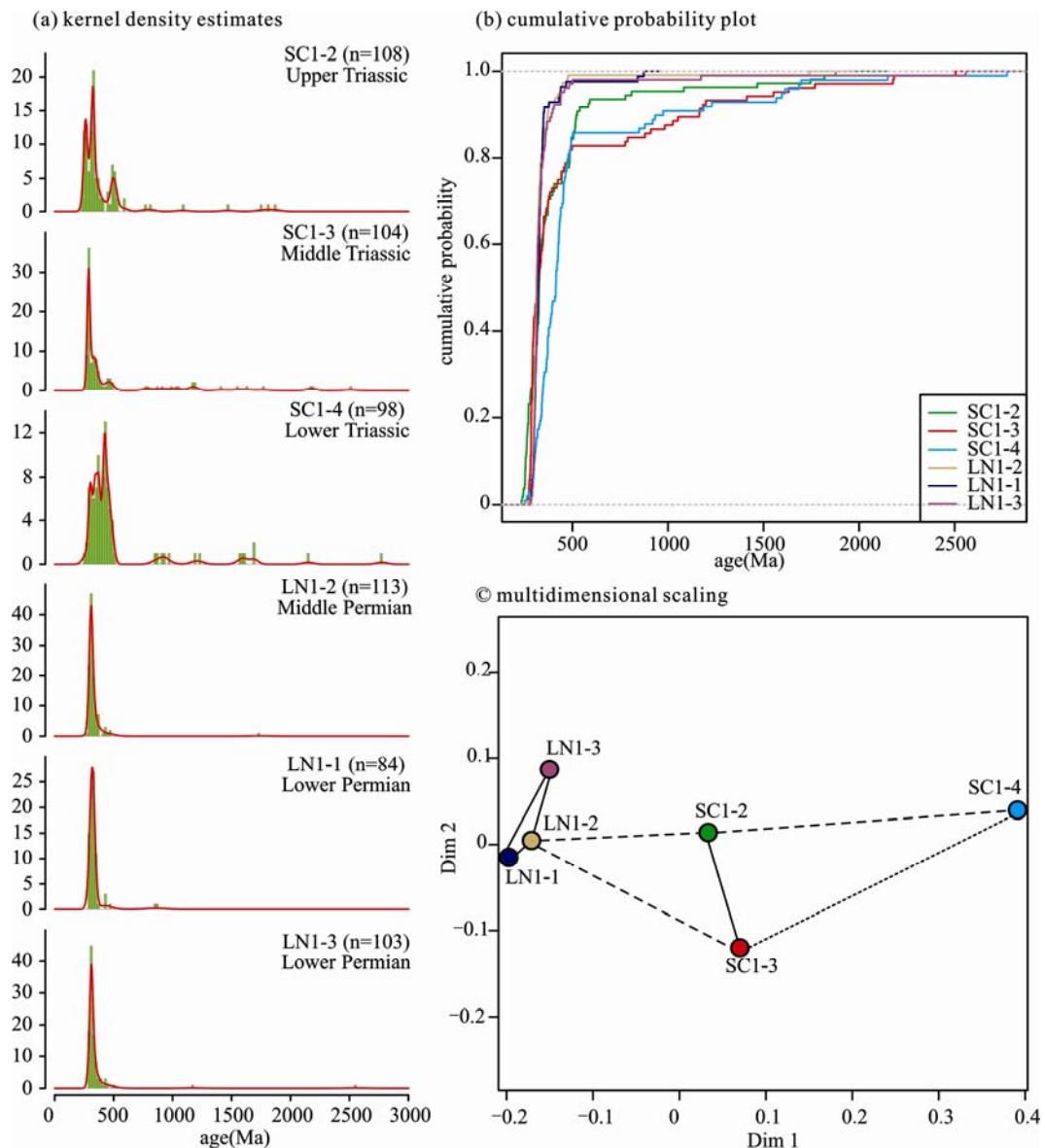


Fig. 7. (a) Detrital zircon KDE diagrams, (b) CPP plot, and (c) MDS plot showing significant changes in the source-to-sink system from the Permian to the Triassic.

MDS plot groups the samples with similar age spectra, with solid and dashed lines marking the closest and the second closest neighbors, respectively. The Permian data are sourced from Zhang et al. (2019b). The data were plotted using IsoplotsR (Vermeesch 2018).

2017), contact thermal metamorphism (Mao et al., 2015), exhumation (Gillespie et al., 2017; Yin et al., 2018), endogenous metallization (Wu et al., 2017a and references therein; Zhu, 2007 and references therein), and strike-slip deformation (Chen et al., 2005; Wang et al., 2010; Lei et al., 2018) have been found in the Eastern Tianshan and its periphery during the last years (Fig. 8), which provides solid evidence for Indosinian tectonic reactivation. Unfortunately, the corresponding sedimentary record has not been found (Zhu, 2007). In this study, detrital zircon age spectra of the Triassic samples from Well SC1 in the southern Turpan-Hami Basin show obvious inter-sample variability, providing sedimentary evidence for Indosinian tectonic reactivation in the Eastern Tianshan and its

periphery (Fig. 8). Furthermore, the Triassic provenance variation in the Turpan-Hami Basin could be attributed to differential exhumation of different sources driven by coeval strike-slip tectonics along deep faults in the Eastern Tianshan (Fig. 8).

On a broader scale, the Indosinian tectonic reactivation in the Eastern Tianshan was temporally related to the tectonic contraction and inversion initiated in the Late Permian, and they both acted as far-field responds to the continental accretion occurring along the southern Eurasian margin although they exhibited different tectonic behaviors (Hendrix et al., 1992). In detail, the tectonic contraction and inversion initiated in the Late Permian caused crustal thickening and tectonic exhumation in the

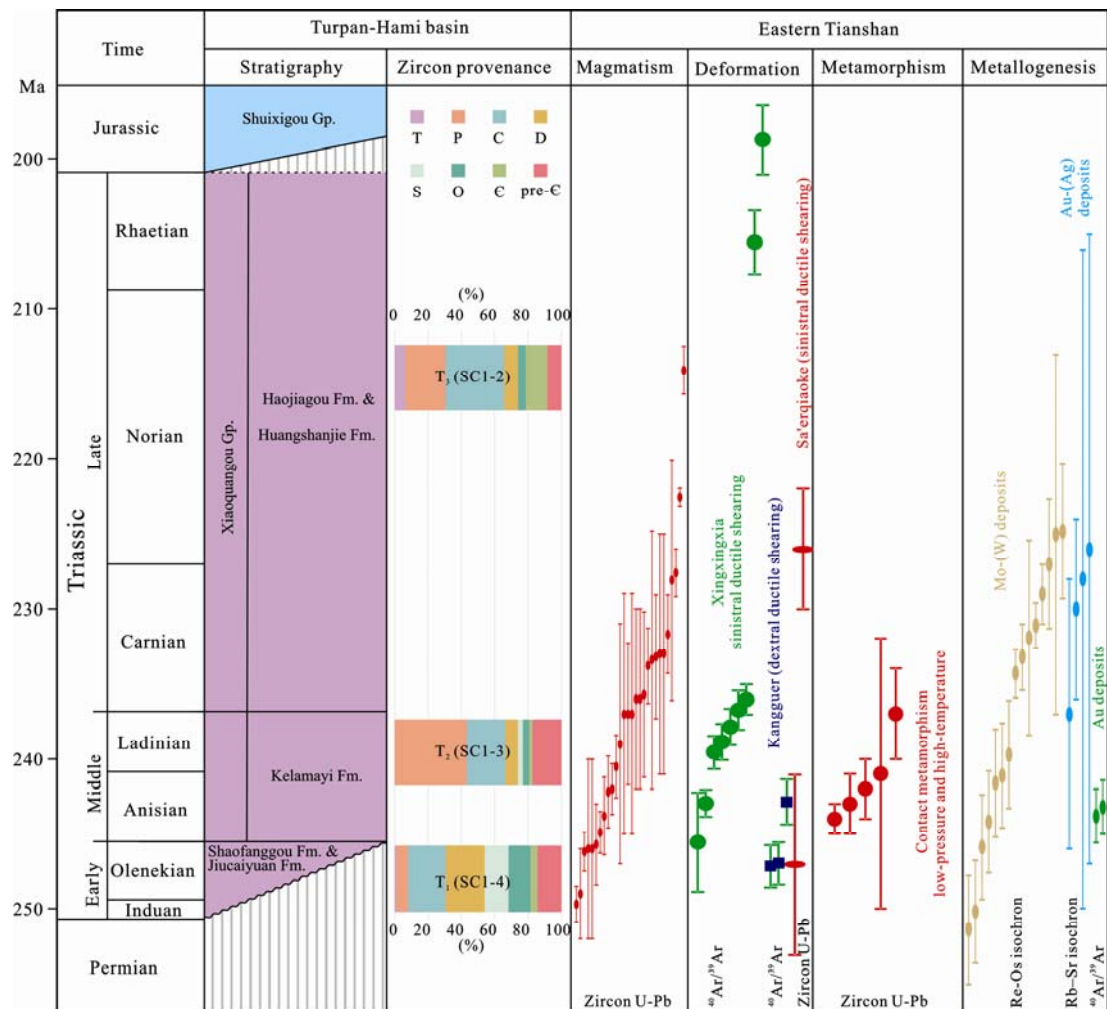


Fig. 8. Composite diagram showing the Indosinian tectonic reactivation in the Eastern Tianshan and its periphery. See text for discussion and data source.

Eastern Tianshan and its periphery, which acted as a respond to the convergence between the Songpan-Ganzi terrane and paleo-Eurasian plate (Dewey et al., 1988; Hendrix et al., 1992). Subsequently, the Triassic subduction-accretion processes, which combinated the Qiangtang Terrane to the paleo-Eurasian plate along the Jinsha Suture (Dewey et al., 1988), propagated tectonic stress to the interior of paleo-Eurasian plate. As a result, the pre-thickened crust of the Eastern Tianshan underwent partial melting (Wu et al., 2017b; Zhang et al., 2017a), and then formed Indosinian plutons and accompanying endogenous deposits (Zhu, 2007; Wu et al., 2017a) as well as low-pressure and high-temperature granulites generated by contact thermal metamorphism (Mao et al., 2015). Meanwhile, significant strike-slip deformation occurred along deep faults (Chen et al., 2005; Wang et al., 2010; Lei et al., 2018) in the Eastern Tianshan, and adjacent sedimentary basins subsided again (Li et al., 1997). Furthermore, the Indosinian plutons in the Eastern Tianshan experienced a rapid emplacement-exhumation process due to coevally persistent strike-slip deformation along deep faults. It is worth to point out that sinistral and

dextral strike-slip deformations coexisted in the Eastern Tianshan and its periphery during the Triassic, and the sinistral deformations along the Xingxing Fault in the south part were genetically related to the Triassic sinistral shearing of the Altyn Tagh Fault System (Wang et al., 2010), while the dextral deformations along the Kangguer Shear Zone in the north part should be resulted from the Triassic counterclockwise rotation of Junggar block (Choulet et al., 2013; Yu et al., 2016). Collectively, we suggest that Indosinian tectonic behavior in the Eastern Tianshan, characterized by partial melting of the pre-thickened crust and strike-slip deformation, is a far-field respond to the coeval continental accretion occurring along the southern Eurasian margin.

## 6 Conclusions

Based on detrital zircon U-Pb geochronological analyses on the subsurface Triassic samples from the Turpan-Hami Basin and synthesis of regional studies, we draw the following conclusions:

- (1) The detrital zircon age spectra of the Triassic

samples from Well SC1 in the Turpan-Hami Basin are obviously different, reflecting significant provenance variability. The zircon grains in the Lower Triassic sample SC1-4 were mainly sourced from the Central Tianshan, and the Jueluotag act as a minor provenance. By contrast, the Late Paleozoic rocks in the Jueluotag act as the main provenance for the Middle-Upper Triassic sample SC1-3 and sample SC1-2, and the Central Tianshan act as a minor provenance. Furtherly, zircon grains in the Middle Triassic sample SC1-3 were mainly sourced from the Permian rocks in the Jueluotag, while Indosinian rapid exhumation brought deeper Carboniferous rocks of the Jueluotag as an important age population for the Upper Triassic sample SC1-2.

(2) Our new subsurface detrital zircon U-Pb data, together with previously reported data in the Turpan-Hami Basin, demonstrate that there are significant changes in the source-to-sink system from the Permian to the Triassic, suggesting that the Permian-Triassic unconformity in the Eastern Tianshan and its periphery is generated by the Late Permian-Early Triassic tectonic contraction and inversion rather than an increasingly arid climate.

(3) The inter-sample variability of detrital zircon age spectra of the Triassic samples from Well SC1 in the southern Turpan-Hami Basin firstly provides sedimentary evidence for Indosinian tectonic reactivation in the Eastern Tianshan and its periphery. The Triassic provenance variation in the Turpan-Hami Basin could be attributed to differential exhumation of different sources driven by coeval strike-slip tectonics along deep faults in the Eastern Tianshan. The Indosinian tectonic behavior in the Eastern Tianshan, which is characterized by partial melting of the pre-thickened crust and strike-slip deformation, acted as a far-field respond to the coeval continental accretion occurring along the southern Eurasian margin.

## Acknowledgments

We thank the PetroChina Turpan-Hami Oilfield Company for kindly providing their subsurface datasets and core samples. We are grateful to Yanguang Li from MLR Key Laboratory of Genesis and Exploration of Magmatic Ore Deposits, Xi'an Center of Geological Survey for his helping on LA-ICP-MS U-Pb dating. We thank the anonymous reviewer and the Editor for their comments and suggestions, which significantly improved the quality of the manuscript. This work was supported by the Science and Technology Program of Shaanxi Province (Grants No. 2019KJXX-078), the National Natural Science Foundation of China (Grants No. 41330315, 41572102, and 41202077), Natural Science Foundation of Shaanxi Province (Grants No. 2018JM4001) and China Geological Survey project (Grants No. 121201011000161111-02).

Manuscript received Aug. 1, 2018  
accepted Dec. 20, 2018  
associate EIC YANG Jingsui  
edited by LIU Lian

## References

- Allen, M.B., Windley, B.F., Zhang, C., Zhao, Z.Y., and Wang, G.R., 1991. Basin evolution within and adjacent to the Tien Shan Range, NW China. *Journal of the Geological Society*, 148(2): 369–378.
- Bai, B., Zhou, L.F., Zou, C.N., Zhu, R.K., Liu, H.W., Liu, Z., Gao, J.P., and Yang, W.J., 2010. Definition of some unconformities in the south margin of Junggar Basin, NW China. *Petroleum Exploration and Development*, 37(3): 270–280 (in Chinese with English abstract).
- Belousova, E.A., Griffin, W.L., O'Reilly, S.Y., and Fisher, N.I., 2002. Igneous zircon: Trace element composition as an indicator of source rock type. *Contributions to Mineralogy and Petrology*, 143(5): 602–622.
- Carroll, A.R., Liang, Y.L., Graham, S.A., Xiao, X.C., Hendrix, M.S., Chu, J.C., and McKnight, C. L., 1990. Junggar basin, northwest China: trapped Late Paleozoic ocean. *Tectonophysics*, 181(1–4): 1–14.
- Cawood, P.A., Hawkesworth, C.J., and Dhuime, B., 2012. Detrital zircon record and tectonic setting. *Geology*, 40(10): 875–878.
- Chen, W., Sun, S., Zhang, Y., Xiao, W.J., Wang, Y.T., Wang, Q.L., Jiang, L.F., and Yang, J.T., 2005.  $^{40}\text{Ar}/^{39}\text{Ar}$  geochronology of the Qiugemingtashi - Huangshan ductile shear zone in East Tianshan, Xinjiang, NW China. *Acta Geologica Sinica*, 79(6): 790–804 (in Chinese with English abstract).
- Chen, K., Gumiaux, C., Augier, R., Chen, Y., Wang, Q., Lin, W., and Wang, S., 2011. The Mesozoic palaeorelief of the northern Tian Shan (China). *Terra Nova*, 23(3): 195–205.
- Chen, K., Lin, W., and Wang, Q., 2015. The Bogeda Shan uplifting: Evidence from multiple phases of deformation. *Journal of Asian Earth Sciences*, 99(2): 1–12.
- Choulet, F., Chen, Y., Cogné, J.P., Rabillard, A., Wang, B., Lin, W., Faure, M., and Cluzel, D., 2013. First Triassic palaeomagnetic constraints from Junggar (NW China) and their implications for the Mesozoic tectonics in Central Asia. *Journal of Asian Earth Sciences*, 78(12): 371–394.
- Coleman, R.G., 1989. Continental growth of northwest China. *Tectonics*, 8(3): 621–635.
- Corfu, F., 2003. Atlas of Zircon Textures. *Reviews in Mineralogy and Geochemistry*, 53(1): 469–500.
- Dewey, J.F., Shackleton, R.M., Chang, C., and Sun, Y., 1988. The Tectonic Evolution of the Tibetan Plateau. *Philosophical Transactions of the Royal Society A: Mathematical, Physical and Engineering Sciences*, 327(1594): 379–413.
- Dickinson, W.R., and Gehrels, G.E., 2009. Use of U-Pb ages of detrital zircons to infer maximum depositional ages of strata: A test against a Colorado Plateau Mesozoic database. *Earth and Planetary Science Letters*, 288(1–2): 115–125.
- Du, Q.X., Han, Z.Z., Shen, X.L., Han, C., Song, Z.G., Gao, L.H., Han, M., Zhong, W.J., and Yan, J.L., 2017. New Evidence of Detrital Zircon Ages for the Final Closure Time of the Paleo-Asian Ocean in the Eastern Central Asian Orogenic Belt (NE China). *Acta Geologica Sinica (English Edition)*, 91(5): 1910–1914.
- Dumitru, T.A., Zhou, D., Chang, E.Z., Graham, S.A., Hendrix, M.S., Sobel, E.R., and Carroll, A.R., 2001. Uplift, exhumation, and deformation in the Chinese Tian Shan. In: Hendrix, M.S., and Davis, G.A. (eds.), *Paleozoic and Mesozoic Tectonic Evolution of Central and Eastern Asia: From Continental Assembly to Intracontinental Deformation*. Geological Society of America, Memoir 194: 71–99.
- Fang, Y., Wu, C., Guo, Z., Hou, K., Dong, L., Wang, L., and Li, L., 2015. Provenance of the southern Junggar Basin in the Jurassic: Evidence from detrital zircon geochronology and depositional environments. *Sedimentary Geology*, 315: 47–63.
- Fedo, C. M., 2003. Detrital Zircon Analysis of the Sedimentary Record. *Reviews in Mineralogy and Geochemistry*, 53(1): 277–303.
- Gao, G., Yang, S., Liang, H., Wang, Z., and Li, X., 2018. The origin and secondary alteration of dissolved gas in oil: A case study from the western Tu-Ha Basin, China. *Journal of Natural Gas Science and Engineering*, 52: 283–294.
- Gao, J., and Klemd, R., 2003. Formation of HP-LT rocks and their tectonic implications in the western Tianshan Orogen, NW China: Geochemical and age constraints. *Lithos*, 66(1–2):

- 1–22.
- Gao, J., Long, L., Klemd, R., Qian, Q., Liu, D., Xiong, X., Su, W., Liu, W., Wang, Y., and Yang, F., 2009. Tectonic evolution of the South Tianshan orogen and adjacent regions, NW China: geochemical and age constraints of granitoid rocks. *International Journal of Earth Sciences*, 98(6): 1221–1238.
- Gehrels, G., 2014. Detrital Zircon U-Pb Geochronology Applied to Tectonics. *Annual Review of Earth and Planetary Sciences*, 42(1): 127–149.
- Gillespie, J., Glorie, S., Jepson, G., Zhang, Z.Y., Xiao, W.J., Danišik, M., and Collins, A.S., 2017. Differential exhumation and crustal tilting in the easternmost Tianshan (Xinjiang, China), revealed by low-temperature thermochronology. *Tectonics*, 36(10): 2142–2158.
- Graham, S.A., Hendrix, M.S., Wang, L.B., and Carroll, A.R., 1993. Collisional successor basins of western China: Impact of tectonic inheritance on sand composition. *Geological Society of America Bulletin*, 105(3): 323–344.
- Greene, T.J., Carroll, A.R., Hendrix, M.S., Graham, S.A., Wartes, M.A., and Abbink, O.A., 2001. Sedimentary record of Mesozoic deformation and inception of the Turpan-Hami basin, northwest China. *Geological Society of America Memoirs* 194: 317–340.
- Greene, T.J., Carroll, A.R., Wartes, M., Graham, S.A., and Wooden, J.L., 2005. Integrated Provenance Analysis of a Complex Orogenic Terrane: Mesozoic Uplift of the Bogda Shan and Inception of the Turpan-Hami Basin, NW China. *Journal of Sedimentary Research*, 75(2): 251–267.
- Gu, L.X., Hu, S.X., Yu, C.S., Li, H.Y., Xiao, X.J., and Yan, Z.F., 2000. Carboniferous volcanites in the Bogda orogenic belt of eastern Tianshan: their tectonic implications. *Acta Petrologica Sinica*, 16(3): 305–316 (in Chinese with English abstract).
- Han, B.F., Guo, Z.J., Zhang, Z.C., Zhang, L., Chen, J.F., and Song, B., 2010. Age, geochemistry, and tectonic implications of a late Paleozoic stitching pluton in the North Tian Shan suture zone, western China. *Geological Society of America Bulletin*, 122(3–4): 627–640.
- Han, S., Zhang, J., Zhou, Y., Bai, S., Huang, L., Wang, C., and Huang, W., 2016a. Formation and accumulation of lower Jurassic tight gas sands field in Kekeya area of Tuha Basin, northwestern China. *Journal of Natural Gas Science and Engineering*, 29: 101–109.
- Han, Y., and Zhao, G., 2018. Final amalgamation of the Tianshan and Junggar orogenic collage in the southwestern Central Asian Orogenic Belt: Constraints on the closure of the Paleo-Asian Ocean. *Earth-Science Reviews*, 186: 129–152.
- Han, Y., Zhao, G., Sun, M., Eizenhöfer, P.R., Hou, W., Zhang, X., Liu, D., and Wang, B., 2016b. Detrital zircon provenance constraints on the initial uplift and denudation of the Chinese western Tianshan after the assembly of the southwestern Central Asian Orogenic Belt. *Sedimentary Geology*, 339: 1–12.
- He, Z., Wang, B., Zhong, L., and Zhu, X., 2018. Crustal evolution of the Central Tianshan Block: Insights from zircon U-Pb isotopic and structural data from meta-sedimentary and meta-igneous rocks along the Wulasitai – Wulanmoren shear zone. *Precambrian Research*, 314: 111–128.
- Hendrix, M.S., Dumitru, T.A., and Graham, S.A., 1994. Late Oligocene-early Miocene unroofing in the Chinese Tian Shan: An early effect of the India-Asia collision. *Geology*, 22(6): 487–490.
- Hendrix, M.S., Graham, S.A., Carroll, A.R., Sobel, E.R., McKnight, C.L., Schulein, B.J., and Wang, Z., 1992. Sedimentary record and climatic implications of recurrent deformation in the Tian Shan: evidence from Mesozoic strata of the north Tarim, south Junggar, and Turpan basins, northwest China. *Geological Society of America Bulletin*, 104 (1): 53–79.
- Hu, A., Jahn, B.M., Zhang, G., Chen, Y., and Zhang, Q., 2000. Crustal evolution and Phanerozoic crustal growth in northern Xinjiang: Nd isotopic evidence. Part I. Isotopic characterization of basement rocks. *Tectonophysics*, 328(1–2): 15–51.
- Huang, B., Fu, D., Kusky, T., Ruan, K., Zhou, W., and Zhang, X., 2018. Sedimentary provenance in response to Carboniferous arc-basin evolution of East Junggar and North Tianshan belts in the southwestern Central Asian Orogenic Belt. *Tectonophysics*, 722: 324–341.
- Huang, Z., Long, X., Kröner, A., Yuan, C., Wang, Y., Chen, B., and Zhang, Y., 2015. Neoproterozoic granitic gneisses in the Chinese Central Tianshan Block: Implications for tectonic affinity and Precambrian crustal evolution. *Precambrian Research*, 269: 73–89.
- Ji, H., Tao, H., Wang, Q., Qiu, Z., Ma, D., Qiu, J., and Liao, P., 2018. Early to Middle Jurassic tectonic evolution of the Bogda Mountains, Northwest China: Evidence from sedimentology and detrital zircon geochronology. *Journal of Asian Earth Sciences*, 153: 57–74.
- Jiang, S., Li, S., Somerville, I.D., Lei, J., and Yang, H., 2015. Carboniferous-Permian tectonic evolution and sedimentation of the Turpan-Hami Basin, NW China: Implications for the closure of the Paleo-Asian Ocean. *Journal of Asian Earth Sciences*, 113: 644–655.
- Jolivet, M., Dominguez, S., Charreau, J., Chen, Y., Li, Y., and Wang, Q., 2010. Mesozoic and Cenozoic tectonic history of the central Chinese Tian Shan: reactivated tectonic structures and active deformation. *Tectonics*, 29(6): TC6019.
- Kuang, L.C., Zhang, Y.Q., Zha, M., Chen, Z.H., Li, L., Kong, Y.H., and Zhang, Y., 2013. Carboniferous tectonic setting and evolution in northern Xinjiang, China. *Acta Geologica Sinica*, 87(3): 311–320 (in Chinese with English abstract).
- Lei, W., Guo, J., Chen, D., Chu, J., and Li, Y., 2018. Ductile shearing and LA-ICP MS zircon U-Pb dating of Sa'erqiaoke ductile shear belt in the Bogda orogen: Constraints on the process of mountain building of eastern Tianshan. *Geological Journal* (In press).
- Li, W.H., Zhou, L.F., Liu, Y.Q., Liang, S.J., and Long, D.J., 1997. Evolution of sedimentary framework and environment of Turpan-Hami basin. *Xinjiang Petroleum Geology*, 18(2): 135–141 (in Chinese with English abstract).
- Li, Z., and Peng, S.T., 2013. U-Pb geochronological records and provenance system analysis of the Mesozoic-Cenozoic sandstone detrital zircons in the northern and southern piedmonts of Tianshan, Northwest China: Responses to intracontinental basin-range evolution. *Acta Petrologica Sinica*, 29(3): 739–755 (in Chinese with English abstract).
- Liao, Z.T., Chen, Z.Q., and Liu, L.J., 2011. Two Stratigraphic Concerns on the Central and Northern Tianshan Tectonic Complex, Northwest China. *Acta Geologica Sinica*, 85(6): 925–937 (in Chinese with English abstract).
- Liu, D.D., Guo, Z.J., and Zhang, Z.Y., 2013. A new viewpoint of the Aiweiergou unconformity, Northern Tian Shan, Xinjiang. *Geotectonica ET Metallogenesis*, 37(3): 349–365 (in Chinese with English abstract).
- Liu, D., Zhang, C., Yao, E., Song, Y., Jiang, Z., and Luo, Q., 2017. What generated the Late Permian to Triassic unconformities in the southern Junggar Basin and western Turpan Basin: tectonic uplift, or increasing aridity? *Palaeogeography, Palaeoclimatology, Palaeoecology*, 468: 1–17.
- Liu, H.Q., Xu, Y.G., Wei, G.J., Wei, J.X., Yang, F., Chen, X.Y., Liu, L., and Wei, X., 2016. B isotopes of Carboniferous-Permian volcanic rocks in the Tuha basin mirror a transition from subduction to intraplate setting in Central Asian Orogenic Belt. *Journal of Geophysical Research: Solid Earth*, 121(11): 7946–7964.
- Ludwig, K., 2012. User's manual for Isoplot version 3.75–4.15: a geochronological toolkit for Microsoft Excel. *Berkley Geochronological Center Special Publication* 5: 1–75.
- Ma, D.L., Pan, J.G., Zhang, H.Q., Wang, H.B., Wang, Y.J., Wei, C.R., and Chen, X.Z., 2018. The geometry and kinematic characteristics of T/P syn-tectonic unconformities at Xiaoquzi anticline and its geological significance to tectonic evolution at the south margin of Junggar Basin. *Chinese Journal of Geology*, 53(1): 146–154 (in Chinese with English abstract).
- Ma, X., Shu, L., Meert, J.G., and Li, J., 2014. The Paleozoic evolution of Central Tianshan: Geochemical and geochronological evidence. *Gondwana Research*, 25(2): 797–819.
- Mao, L.J., He, Z.Y., Zhang, Z.M., Klemd, R., Xiang, H., Tian, Z.L., and Zong, K.Q., 2015. Origin and geodynamic

- significance of the early Mesozoic Weiya LP and HT granulites from the Chinese Eastern Tianshan. *Lithos*, 239: 142–156.
- Şengör, A.M.C., Natal'in, B.A., and Burtman, V.S., 1993. Evolution of the Altaiid tectonic collage and Palaeozoic crustal growth in Eurasia. *Nature*, 364(6435): 299–307.
- Shao, L., Stattegger, K., and Garbe-Schoenberg, C.D., 2001. Sandstone Petrology and Geochemistry of the Turpan Basin (NW China): Implications for the Tectonic Evolution of a Continental Basin. *Journal of Sedimentary Research*, 71(1): 37–49.
- Shao, L., Stattegger, K., Li, W., and Haupt, B.J., 1999. Depositional style and subsidence history of the Turpan Basin (NW China). *Sedimentary Geology*, 128(1–2): 155–169.
- Shao, L., Zhang, P., Hilton, J., Gayer, R., Wang, Y., Zhao, C., and Luo, Z., 2003. Paleoenvironments and paleogeography of the Lower and lower Middle Jurassic coal measures in the Turpan-Hami oil-prone coal basin, northwestern China. *AAPG Bulletin*, 87(2): 335–355.
- Shu, L.S., Charvet, J., Guo, L.Z., Lu, H.F., and Laurent-Charvet, S., 1999. A Large-Scale Palaeozoic Dextral Ductile Strike-Slip Zone: the Aqqikudug-Weiye Zone along the Northern Margin of the Central Tianshan Belt, Xinjiang, NW China. *Acta Geologica Sinica (English Edition)*, 73(2): 148–162.
- Shu, L., Wang, B., Zhu, W., Guo, Z., Charvet, J., and Zhang, Y., 2011. Timing of initiation of extension in the Tianshan, based on structural, geochemical and geochronological analyses of bimodal volcanism and olistostrome in the Bogda Shan (NW China). *International Journal of Earth Sciences*, 100(7): 1647–1663.
- Su, C.Q., Sun, Y.J., Yang, X.K., and Xu, A.D., 2006. Definition of some unconformities in the Late Paleozoic-Mesozoic system in the Houxia-Ewirgol area, Tianshan Mountains, and its geological significance. *Geological Bulletin of China*, 25(8): 977–985 (in Chinese with English abstract).
- Tang, W., Zhang, Z., Li, J., Li, K., Chen, Y., and Guo, Z., 2014. Late Paleozoic to Jurassic tectonic evolution of the Bogda area (northwest China): Evidence from detrital zircon U-Pb geochronology. *Tectonophysics*, 626(1): 144–156.
- Tang, W., Zhang, Z., Li, J., Li, K., Luo, Z., and Chen, Y., 2015. Mesozoic and Cenozoic uplift and exhumation of the Bogda Mountain, NW China: Evidence from apatite fission track analysis. *Geoscience Frontiers*, 6(4): 617–625.
- Tao, M.X., 2010. The two kinds of tectonic unit systems in Turpan-Hami Basin Xinjiang China. *Geological Bulletin of China*, 29(2/3): 297–304 (in Chinese with English abstract).
- Tappognier, P., and Molnar, P., 1979. Active faulting and cenozoic tectonics of the Tien Shan, Mongolia, and Baykal Regions. *Journal of Geophysical Research: Solid Earth*, 84(B7): 3425–3459.
- Thomas, W.A., 2011. Detrital-zircon geochronology and sedimentary provenance. *Lithosphere*, 3(4): 304–308.
- Tian, J., Liu, J., Zhang, Z., and Cong, F., 2017. Hydrocarbon-generating potential, depositional environments, and organisms of the Middle Permian Tarlong Formation in the Turpan-Hami Basin, northwestern China. *GSA Bulletin*, 129(9–10): 1252–1265.
- Tian, Z., Sun, J., Windley, B.F., Zhang, Z., Gong, Z., Lin, X., and Xiao, W., 2016. Cenozoic detachment folding in the southern Tianshan foreland, NW China: Shortening distances and rates. *Journal of Structural Geology*, 84: 142–161.
- Vermeesch, P., 2018. IsoplotR: A free and open toolbox for geochronology. *Geoscience Frontiers*, 9(5): 1479–1483.
- Wali, G., Wang, B., Cluzel, D., and Zhong, L., 2018. Carboniferous – Early Permian magmatic evolution of the Bogda Range (Xinjiang, NW China): Implications for the Late Paleozoic accretionary tectonics of the SW Central Asian Orogenic Belt. *Journal of Asian Earth Sciences*, 153: 238–251.
- Wang, J.L., Wu, C.D., Zhu, W., Li, Z., Wu, J., Chen, R., and Wang, J., 2016. Tectonic-depositional environment and prototype basin evolution of the Permian-Triassic in the southern Junggar Basin. *Journal of Palaeogeography*, 18(4): 643–660 (in Chinese with English abstract).
- Wang, B., Cluzel, D., Jahn, B.M., Shu, L., Chen, Y., Zhai, Y., Branquet, Y., Barbanson, L., and Sizaret, S., 2014. Late Paleozoic pre- and syn-kinematic plutons of the Kangguer-huangshan shear zone: Inference on the tectonic evolution of the eastern Chinese north Tianshan. *American Journal of Science*, 314(1): 43–79.
- Wang, J., Cao, Y., Wang, X., Liu, K., Wang, Z., and Xu, Q., 2018a. Sedimentological constraints on the initial uplift of the West Bogda Mountains in Mid-Permian. *Scientific Reports*, 8(1): 1453.
- Wang, M., Zhang, J., and Liu, K., 2015. Continuous denudation and pediplanation of the Chinese Western Tianshan orogen during Triassic to Middle Jurassic: Integrated evidence from detrital zircon age and heavy mineral chemical data. *Journal of Asian Earth Sciences*, 113: 310–324.
- Wang, Q., Li, S., and Du, Z., 2009. Differential uplift of the Chinese Tianshan since the Cretaceous: constraints from sedimentary petrography and apatite fission-track dating. *International Journal of Earth Sciences*, 98(6): 1341–1363.
- Wang, X.S., Gao, J., Klemd, R., Jiang, T., Li, J.L., Zhang, X., and Xue, S.C., 2017. The Central Tianshan Block: A microcontinent with a Neoproterozoic basement in the southwestern Central Asian Orogenic Belt. *Precambrian Research*, 295: 130–150.
- Wang, Y., Jia, D., Pan, J., Wei, D., Tang, Y., Wang, G., Wei, C., and Ma, D., 2018b. Multiple-phase tectonic superposition and reworking in the Junggar Basin of northwestern China—Implications for deep-seated petroleum exploration. *AAPG Bulletin*, 102(8): 1489–1521.
- Wang, Y., Sun, G., and Li, J., 2010. U-Pb (SHRIMP) and  $^{40}\text{Ar}/^{39}\text{Ar}$  geochronological constraints on the evolution of the Xingxingxia shear zone, NW China: A Triassic segment of the Altyn Tagh fault system. *Geological Society of America Bulletin*, 122(3–4): 487–505.
- Wiedenbeck, M., Allé, P., Corfu, F., Griffin, W.L., Meier, M., Oberli, F., Quadt, A.V., Roddick, J.C., and Spiegel, W., 1995. Three natural zircon standards for U - Th - Pb, Lu - Hf, trace element and REE analyses. *Geostandards and Geoanalytical Research*, 19(1): 1–23.
- Windley, B.F., Alexeev, D., Xiao, W., Kroner, A., and Badarch, G., 2007. Tectonic models for accretion of the Central Asian Orogenic Belt. *Journal of the Geological Society*, 164(1): 31–47.
- Windley, B.F., Allen, M.B., Zhang, C., Zhao, Z.Y., and Wang, G.R., 1990. Paleozoic accretion and Cenozoic redeformation of the Chinese Tien Shan Range, central Asia. *Geology*, 18(2): 128–131.
- Wu, T., and Zhao, W., 1997. Formation and distribution of oil and gas fields in Turpan-Hami coal-bearing basin. Beijing: Petroleum Industry Press, 271 (in Chinese with English abstract).
- Wu, L., Jiao, Y., Roger, M., and Yang, S., 2009. Sedimentological setting of sandstone-type uranium deposits in coal measures on the southwest margin of the Turpan-Hami Basin, China. *Journal of Asian Earth Sciences*, 36(2–3): 223–237.
- Wu, Y.S., Chen, Y.J., and Zhou, K.F., 2017a. Mo deposits in Northwest China: Geology, geochemistry, geochronology and tectonic setting. *Ore Geology Reviews*, 81: 641–671.
- Wu, Y.S., Zhou, K.F., Li, N., and Chen, Y.J., 2017b. Zircon U-Pb dating and Sr-Nd-Pb-Hf isotopes of the ore-associated porphyry at the giant Donggebi Mo deposit, Eastern Tianshan, NW China. *Ore Geology Reviews*, 81: 794–807.
- Xia, L.Q., Xia, Z.C., Xu, X.Y., Li, X.M., and Ma, Z.P., 2008. Relative contributions of crust and mantle to the generation of the Tianshan Carboniferous rift-related basic lavas, northwestern China. *Journal of Asian Earth Sciences*, 31(4–6): 357–378.
- Xia, L.Q., Xu, X.Y., Xia, Z.C., Li, X.M., Ma, Z.P., and Wang, L.S., 2004. Petrogenesis of Carboniferous rift-related volcanic rocks in the Tianshan, northwestern China. *Geological Society of America Bulletin*, 116(3): 419.
- Xiao, W.J., Zhang, L.C., Qin, K.Z., Sun, S., and Li, J.L., 2004. Paleozoic accretionary and collisional tectonics of the Eastern Tianshan (China): Implications for the continental growth of central Asia. *American Journal of Science*, 304(4): 370–395.

- Xiao, W., Han, C., Yuan, C., Sun, M., Lin, S., Chen, H., Li, Z., Li, J., and Sun, S., 2008. Middle Cambrian to Permian subduction-related accretionary orogenesis of Northern Xinjiang, NW China: Implications for the tectonic evolution of central Asia. *Journal of Asian Earth Sciences*, 32(2–4): 102–117.
- Xiao, W., Windley, B.F., Allen, M.B., and Han, C., 2013. Paleozoic multiple accretionary and collisional tectonics of the Chinese Tianshan orogenic collage. *Gondwana Research*, 23(4): 1316–1341.
- Xie, W., Xu, Y.G., Luo, Z.Y., Liu, H.Q., Hong, L.B., and Ma, L., 2016. Petrogenesis and geodynamic implications of the Late Carboniferous felsic volcanics in the Bogda belt, Chinese Northern Tianshan. *Gondwana Research*, 39: 165–179.
- Xu, X.W., Li, X.H., Jiang, N., Li, Q.L., Qu, X., Yang, Y.H., Zhou, G., and Dong, L.H., 2015. Basement nature and origin of the Junggar terrane: New zircon U-Pb-Hf isotope evidence from Paleozoic rocks and their enclaves. *Gondwana Research*, 28(1): 288–310.
- Yang, W., Li, J., Guo, Z., Jolivet, M., and Heilbron, G., 2017. New Apatite Fission-Track Ages of the Western Kuqa Depression: Implications for the Mesozoic–Cenozoic Tectonic Evolution of South Tianshan, Xinjiang. *Acta Geologica Sinica* (English Edition), 91(2): 396–413.
- Yang, T.N., Li, J.Y., Wang, Y., and Dang, Y.X., 2009. Late Early Permian (266 Ma) N–S compressional deformation of the Turfan basin, NW China: the cause of the change in basin pattern. *International Journal of Earth Sciences*, 98(6): 1311–1324.
- Yang, Y.T., Guo, Z.X., and Luo, Y.J., 2017. Middle-Late Jurassic tectonostratigraphic evolution of Central Asia, implications for the collision of the Karakoram-Lhasa Block with Asia. *Earth-Science Reviews*, 166, 83–110.
- Yang, Y.T., Song, C.C., and He, S., 2015. Jurassic tectonostratigraphic evolution of the Junggar basin, NW China: A record of Mesozoic intraplate deformation in Central Asia. *Tectonics*, 34(1): 86–115.
- Yu, Y., Wang, X., Rao, G., and Wang, R., 2016. Mesozoic reactivated transpressional structures and multi-stage tectonic deformation along the Hong-Che fault zone in the northwestern Junggar Basin, NW China. *Tectonophysics*, 679: 156–168.
- Zhang, S., Liu, C., Yang, M., Wang, J., Bai, J., and Huang, H., 2019a. Decoding Provenance and Tectonothermal Events by Detrital Zircon Fission-Track and U/Pb Double Dating: A Case of the Southern Ordos Basin. *Acta Geologica Sinica* (English Edition), 93(4): 845–856.
- Zhang, Z., Gu, L., Wu, C., Li, W., Xi, A., and Wang, S., 2005. Zircon SHRIMP dating for the Weiyia pluton, Eastern Tianshan: Its geological implications. *Acta Geologica Sinica* (English Edition): 79(4): 481–490.
- Zhang, S., Wang, J., Liu, C., Bai, J., Peng, H., Huang, H., and Guan, Y., 2019b. Detrital zircon U–Pb geochronology of the Permian strata in the Turpan–Hami Basin in North Xinjiang, NW China: Depositional age, provenance and tectonic implications. *Geological Journal*, 54(2): 1064–1080.
- Zhang, X., Zhao, G., Sun, M., Eizenhöfer, P.R., Han, Y., Hou, W., Wang, B., Liu, Q., and Xu, B., 2016. Tectonic evolution from subduction to arc-continent collision of the Junggar ocean: Constraints from U-Pb dating and Hf isotopes of detrital zircons from the North Tianshan belt, NW China. *Geological Society of America Bulletin*, 128(3–4): 644–660.
- Zhang, X., Zhao, G., Sun, M., Han, Y., and Liu, Q., 2017a. Triassic magmatic reactivation in Eastern Tianshan, NW China: Evidence from geochemistry and zircon U-Pb-Hf isotopes of granites. *Journal of Asian Earth Sciences*, 145: 446–459.
- Zhang, Y., Yuan, C., Long, X., Sun, M., Huang, Z., Du, L., and Wang, X., 2017b. Carboniferous bimodal volcanic rocks in the Eastern Tianshan, NW China: Evidence for arc rifting. *Gondwana Research*, 43: 92–106.
- Zhang, Z.M., Liou, J.G., and Coleman, R.G., 1984. An outline of the plate tectonics of China. *Geological Society of America Bulletin*, 95(3): 295–312.
- Zhao, H.G., Su, R., Liang, J.W., Wang, J., Jin, Y.X., Ou, G.X., and Jiang, X.H., 2017. Petrology, Geochemical Characteristics and Genesis of the Tianhu Pluton in the East Section of the Middle Tianshan Mountains. *Acta Geologica Sinica*, 91(6): 1208–1226 (in Chinese with English abstract).
- Zhao, X.C., Liu, C.Y., Wang, J.Q., Duan, L., Zhao, Y., Zhang, Q.H., and Luo, W., 2017. Petrology, Geochemistry and Zircon U-Pb Geochronology of the Xiangshan Group in the Eastern Hexi Corridor Belt: Implications for Provenance and Tectonic Evolution. *Acta Geologica Sinica* (English Edition), 91(5): 1680–1703.
- Zhao, L., Chen, H., Zhang, L., Zhang, W., Yang, J., and Yan, X., 2018. The Late Paleozoic magmatic evolution of the Aqishan-Yamansu belt, Eastern Tianshan: Constraints from geochronology, geochemistry and Sr–Nd–Pb–Hf isotopes of igneous rocks. *Journal of Asian Earth Sciences*, 153: 170–192.
- Zhao, X., Liu, C., Wang, J., Zhao, Y., Wang, L., and Zhang, Q., 2016. Detrital zircon U-Pb ages of Paleozoic sedimentary rocks from the eastern Hexi Corridor Belt (NW China): Provenance and geodynamic implications. *Sedimentary Geology*, 339: 32–45.
- Zheng, J., Sun, M., Zhao, G., Robinson, P.T., and Wang, F., 2007. Elemental and Sr-Nd-Pb isotopic geochemistry of Late Paleozoic volcanic rocks beneath the Junggar basin, NW China: Implications for the formation and evolution of the basin basement. *Journal of Asian Earth Sciences*, 29(5–6): 778–794.
- Zhu W., Wu C.D., Wang J.L., Chen R., Wu J., and Zhou T.Q., 2017. Triassic Provenance and Its Tectonic Significance in Sikeshu Sag, Junggar Basin. *Xinjiang Petroleum Geology*, 38 (5): 512–518 (in Chinese with English abstract).
- Zhu Y.F., 2007. Indosian movement and metallogeny in Xinjiang, China. *Geological Bulletin of China*, 26(5): 510–519 (in Chinese with English abstract).

#### About the first author



ZHANG Shaohua, male, born in 1990 in Baoji City, Shaanxi Province, China. He is now a lecturer of Xi'an Shiyou University. His current research interests include basin analysis, regional tectonics, and petroleum geology. E-mail: zhangshh86@163.com.

#### About the Corresponding author



LIU Chiyang, male, born in 1953 in Xi'an City, Shaanxi Province, China. He is currently a professor of Northwest University (China). He received his B.Sc. and M.Sc. degrees from Northwest University (China). His academic research career spans almost 40 years in the fields of basin analysis and petroleum geology. E-mail: lcy@nwu.edu.cn.